Metallic networks and hydrogen compensation in highly nonstoichiometric amorphous In$_2$O$_{3-x}$

J. E. Medvedeva ●,[*] E. Caputa-Hatley, and I. Zhuravlev

Department of Physics, Missouri University of Science and Technology, Rolla, Missouri 65409, USA

The unique response of amorphous ionic oxides to changes in oxygen stoichiometry is investigated using computationally intensive *ab initio* molecular dynamics simulations, comprehensive structural analysis, and hybrid density-functional calculations for the oxygen defect formation energy and electronic properties of amorphous In$_2$O$_{3-x}$ with $x = 0$–0.185. In marked contrast to nonstoichiometric crystalline nanocomposites with clusters of metallic inclusions inside an insulating matrix, the lack of oxygen in amorphous indium oxide is distributed between a large fraction of undercoordinated In atoms, leading to an extended shallow state for $x < 0.037$, a variety of weakly and strongly localized states for $0.074 < x < 0.148$, and a percolation-like network of single-atom chains of metallic In-In bonds for $x > 0.185$. The calculated carrier concentration increases from 3.3×10^{20} cm^{-3} at $x = 0.037$ to 6.6×10^{20} cm^{-3} at $x = 0.074$ and decreases only slightly at lower oxygen content. At the same time, the density of deep defects located between 1 and 2.5 eV below the Fermi level increases from 0.4×10^{21} cm^{-3} at $x = 0.074$ to 2.2×10^{21} cm^{-3} at $x = 0.185$. The wide range of localized gap states associated with various spatial distributions and individual structural characteristics of undercoordinated In is passivated by hydrogen that helps enhance electron velocity from 7.6×10^4 to 9.7×10^4 m/s and restore optical transparency within the visible range; H doping is also expected to improve the material's stability under thermal and bias stress.

I. INTRODUCTION

Stoichiometry in metal oxides serves as a primary tool to manipulate the optical and electrical properties of these versatile materials. In post-transition-metal oxides, commonly known as transparent conducting oxides, oxygen deficiency is 10^{18}–10^{19} cm^{-3} even under equilibrium deposition conditions in an ambient environment due to a weak metal-oxygen bonding, ionic in nature. As a result, these materials have relatively low enthalpy of formation, making it easy to manipulate the oxygen-to-metal ratio during the deposition process and/or with a postdeposition treatment and hence to optimize their properties for a wide range of optoelectronic applications [1–10]. A thorough understanding of the structural and electronic properties of the defects induced by oxygen substoichiometry [11–18] is key to achieving optimal material performance.

Highly nonstoichiometric indium oxide grown in an argon atmosphere was shown to have metallic nanoclusters embedded in a crystalline oxide matrix, increasing both the carrier concentration (to as high as 8×10^{20} cm^{-3}) and the carrier mobility of the material [19]. Formation of metallic nanoclusters was also observed in highly nonstoichiometric In-Sn-O, which showed metallic (In and Sn) conductivity via percolation with a superconducting transition at 6 K [20]. These nanocomposite films were shown to exhibit phase separation between the stoichiometric crystalline oxide with insulating properties and the embedded metallic nanoinclusions [21–23].

Amorphous oxides of posttransition metals [24–26] may offer a way to combine high carrier concentration and good mobility while maintaining a uniform morphology. It has been shown that the disordered indium oxide exhibits crystalline-like electron mobility and two orders of magnitude higher carrier concentration as compared to the crystalline oxide grown under the same oxygen partial pressure [27–29]. This sets the ionic amorphous oxides apart from covalent amorphous materials, e.g., Si-based semiconductors, where disorder leads to a strong electron localization suppressing both the carrier mobility and density [25,26,30], and it opens up new prospects in their technological utilization [31–38].

The unique electrical properties of wide-band-gap amorphous oxide semiconductors have been shown to arise from ionic metal-oxygen bonding [24–26]. Unlike amorphous Si or Ge, SiO$_2$ glasses, or amorphous chalcogenides, all of which have covalent bonding between the nearest neighbors, weaker metal-oxygen interactions in wide-band-gap oxides of posttransition metals lead to strong distortions in the *M*-O polyhedra, broad distributions of the *M*-O coordination numbers, as well as fully suppressed structural features in the radial distribution beyond the next-nearest-neighbor shell in an amorphous phase [27,28,39–41]. Due to the strong distortions in the metal-oxygen polyhedra associated with weak ionic In-O bonding, a direct overlap of the In 5*s* orbitals becomes possible in disordered oxides. The metal-metal bonding was observed earlier in other amorphous post-transition-metal oxides such as In-Ga-Zn-O, Zn-Sn-O, etc. [28,42–50]. The metal-metal pairs resulting in the so-called subgap defects have been proposed for substoichiometric disordered oxides as an alternative to an oxygen vacancy concept

[*]juliaem@mst.edu; http://web.mst.edu/~juliaem

that belongs exclusively to crystalline oxides [29]. Despite the aforementioned theoretical reports on the subject, the interplay between the structural and electronic characteristics of the metallic inclusions is far from being understood. A quantitative analysis of key structural features that enable the formation of metal-metal pairs, determines their distribution within the amorphous oxide matrix, and promotes growth into metallic nanoclusters and/or metallic networks as the oxygen stoichiometry is gradually decreased has been lacking.

In this work, the structural and electronic properties of amorphous indium oxide are systematically studied as a function of oxygen nonstoichiometry using *ab initio* molecular dynamics simulations and accurate electronic structure calculations with a hybrid functional. The work combines computationally intensive simulations that offer statistically reliable results with comprehensive structural analysis that allows one to thoroughly investigate the coordination, interatomic distances, and distortion in individual metal-oxygen polyhedron as well as the polyhedra sharing of metal atoms in amorphous structures with respect to diverse structural environments created by oxygen substoichiometry. Specifically, one of the goals of this work is to establish a connection between individual metal coordination and/or polyhedra distortion and the resulting defect binding energies as well as the degree of electron localization caused by the defect. For the latter, the work employs Bader charge calculations for individual metal atoms that account for nonuniform charge density distribution near the highly distorted undercoordinated and undershared metal atoms. This approach departs from the widespread reliance on the traditional calculations of the density of states or atomic orbital contributions that are based on a fixed cutoff radius near the atoms, hence it may misinterpret the nature of the defect and its localization. This is especially important in ionic oxides with interstitial charge-density distribution [51], and it becomes crucial in disordered oxides with large fractions of undercoordinated atoms or highly distorted metal-oxygen polyhedra and in structures with low density.

In addition, this work considers defect compensation in highly nonstoichiometric amorphous indium oxide with hydrogen, identifying the H defect types (donor In-OH versus acceptor In-H-In) and their role in the structural reconfiguration, and determining the resulting electronic properties of hydrogenated amorphous transparent conductors.

II. COMPUTATIONAL METHODS

The amorphous In_2O_{3-x} structures were obtained using the *ab initio* molecular dynamics (MD) liquid-quench approach as implemented in the Vienna Ab Initio Simulation Package (VASP) [52–55]. The calculations are based on density functional theory (DFT) with periodic boundary conditions [56,57], and they employ the Perdew-Burke-Ernzerhof (PBE) exchange-correlation functional [58,59] within the projector augmented-wave method [60,61]. A stoichiometric cell that consisted of 135 atoms, $In_{54}O_{81}$, was used as the initial structure, which was melted at 3000 K to eliminate any crystalline structure memory. In this work, we used a density of 7.1 g/cm^3 for all amorphous indium oxide structures; this optimal density value was previously found from calculated

energy-volume curves for amorphous $In_{54}O_{80}$ [29]. Density-dependent structural changes in amorphous indium oxide have been studied by directly comparing the calculated and experimentally measured extended x-ray absorption fine structure (EXAFS) spectra, and an excellent agreement for the first and second EXAFS peaks was found, as reported in [62].

To model nonstoichiometric structures with lower oxygen content, oxygen atom(s) were randomly removed from the initial cell. Specifically, in addition to the perfectly stoichiometric case, $In_{54}O_{81} = In_2O_{3.000}$, we studied $In_{54}O_{80} = In_2O_{2.963}$, $In_{54}O_{79} = In_2O_{2.926}$, $In_{54}O_{78} = In_2O_{2.889}$, $In_{54}O_{77} = In_2O_{2.852}$, and $In_{54}O_{76} = In_2O_{2.815}$. The above understoichiometric cells correspond to oxygen defect concentrations of 5.7, 11.5, 17.2, 23.0, and 28.8 × 10^{20} cm^{-3}, respectively. We stress here that the substoichiometric structures of amorphous In_2O_{3-x} (with $x = 0$, 0.037, 0.074, 0.111, 0.148, and 0.185, respectively) were simulated using so-called nonstoichiometric quench, i.e., when the oxygen stoichiometry is set at the melting stage of MD, prior to cooling. This approach was shown [29] to provide lower-energy solutions as compared to a static-DFT calculation where an oxygen "vacancy" is created in an already quenched amorphous structure. The nonstoichiometric quench also yields a better statistical representation of the overall structural morphology in the disordered material as compared to the vacancy calculations in a single amorphous structure. As a result, the nonstoichiometric quench was shown to capture the formation of both shallow defects that produce carriers and localized deep defects that limit carrier mobility via electron trapping or scattering [29].

After the stoichiometry and density adjustments, all structures were subsequently melted at 3000 K for at least 10 ps in order to randomize the specific volume or substoichiometric configuration and to stabilize the total energy. Next, liquid quench simulations were performed as follows. Each structure was cooled to 2500 K at the MD rate of 100 K/ps and then rapidly quenched to 100 K at a rate of 200 K/ps. The initial slower cooling rate helps to avoid the formation of O$_2$ defects; at 2500 K, the second peak in the distribution function (responsible for the medium-range structure) begins to develop, hence the quench rate is increased for temperatures below 2500 K. An energy cutoff of 260 eV and a single Γ-point method were used during melting and quenching processes. Finally, each structure was equilibrated at 300 K for 6 ps with a cutoff energy of 400 eV. All MD simulations for nonstoichiometric amorphous oxides were carried out in the NVT ensemble with the Nose-Hoover thermostat using an integration time step of 2 fs. For H-containing structures, the integration time step is 0.5 fs.

To obtain adequate statistical distributions in the structural and, consequently, the electronic properties, 10 separate MD liquid-quench realizations with the same conditions (initial temperature, quench rate, equilibration) were performed for each oxygen stoichiometry, resulting in 60 independent MD quenches. First, we calculate the enthalpy of formation per atom and plot it as a function of MD steps at room temperature for each realization in order to illustrate that the solutions are stable with no energy drift, Fig. 1. The thermal fluctuations in the energy, i.e., the average changes in the energy squared, are 6–15 times smaller as compared to the kT^2c_v, where c_v is the heat capacity for In_2O_3 at room temperature, suggesting
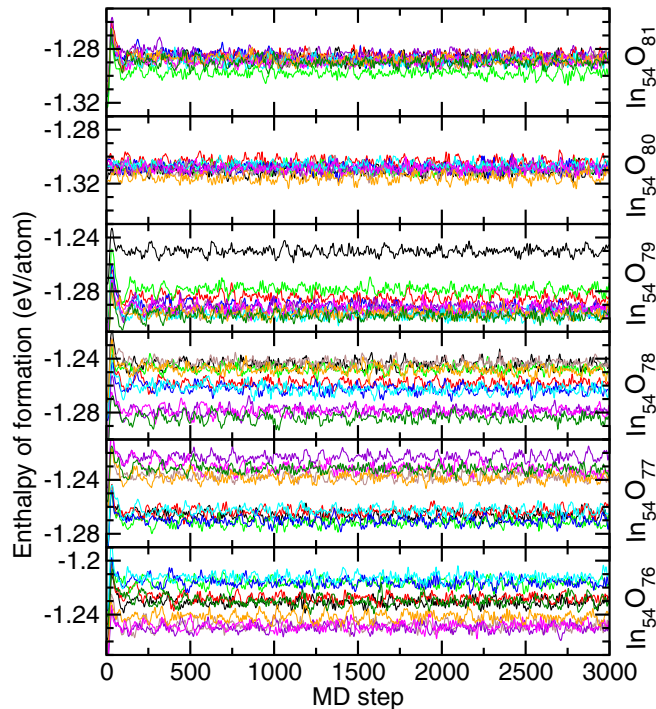
FIG. 1. Enthalpy of formation as a function of MD steps during the equilibration step at 300 K for all amorphous oxides considered in this work.

that configurations are indeed in equilibrium. We note that the energies for 10 realizations are intermixed for the structures with high oxygen content ($In_{54}O_{81}$ and $In_{54}O_{80}$), so that the configuration ensemble represents an amorphous state with a normal distribution of possible energy values. This is consistent with the delocalized nature of the electronic conduction states in $In_{54}O_{81}$ and $In_{54}O_{80}$ reported in this work and in Ref. [29]. In contrast, the structures with lower oxygen content ($In_{54}O_{79}$, $In_{54}O_{78}$, $In_{54}O_{77}$, and $In_{54}O_{76}$) exhibit either bimodal or multimodal energy distributions, Fig. 1. Importantly, the largest energy difference between the modes is about 40 meV/at, which implies that all such configurations are likely to occur in an amorphous state at the specified stoichiometry. The energy difference between the modes represents specific coordination morphology (as will be discussed in detail in this work) with a "frozen" localized state that is stable at room temperature, at least within a time frame of several ps. Indeed, it will be shown later in this work that deep electron traps are formed 2–3 eV below the Fermi level, hence they are stable against thermal fluctuations. It must be pointed out that even larger statistical ensembles are required to predict the density for specific mode(s) or to perform principal component analysis in order to study the underlying mechanisms behind the structural transformations found in this work.

For accurate structural analysis of the crystalline and amorphous oxides, the room-temperature configurations obtained from the MD simulations at 300 K (3000 MD steps resulting in 3000 atomic configurations for each structure) were used. Specifically, the average first-shell In-O distance for each In-O polyhedron (or for the O-In distance in each O-In polyhedron)

is calculated according to [63,64]

$$l_{av} = \frac{\sum_i l_i \exp\left[1 - \left(\frac{l_i}{l_{min}}\right)^6\right]}{\sum_i \exp\left[1 - \left(\frac{l_i}{l_{min}}\right)^6\right]}, \qquad (1)$$

where the summation runs over all oxygen neighbors of a particular metal atom, and l_{min} is the shortest In-O distance in the given In-O polyhedron (or the shortest O-In distance in the given O-In polyhedron). The effective coordination number (ECN) for a metal atom in the In-O polyhedron (or for an oxygen atom in the O-In polyhedron) is then defined as

$$ECN = \sum_i \exp\left[1 - \left(\frac{l_i}{l_{av}}\right)^6\right]. \qquad (2)$$

The contribution to the ECN from a given In-O bond is greater if the In-O bond length (l_i) is shorter than the average In-O distance (l_{av}) in the given In-O polyhedron, and vice versa. For example, in crystalline In_2O_3 with bixbyite structure, the largest contribution to the ECN from an In-O bond is 1.46 (shortest bond), while the smallest is 0.15 (longest bond). Summation of the contributions from all bonds for a given In atom will result in a noninteger ECN value unless all In-O bonds in a polyhedron are identical. In addition, we evaluate the distortion of each In-O polyhedron characterized by the standard deviation of the individual In-O bond length (l_i) from the average In-O bond length (l_{av}) for the given polyhedron. For an ideal polyhedron (i.e., all In-O distances are identical), this parameter is equal to zero. Similarly, the distortion of each O-In polyhedron was calculated. In this work, the average bond length, average effective coordination number, and average distortion were calculated according to the above equations for each atom in each MD configuration and then averaged over the 3000 steps (6 ps) and over the number of MD realizations for each stoichiometry and, in specific cases, over the number of In or O atoms in the cell.

Furthermore, sharing between In-O polyhedra is calculated based on the results of Eqs. (1) and (2). The sharing type, namely face, edge, or corner-sharing that corresponds to three, two, or one oxygen shared between any given pair of In atoms, respectively, is determined for each In-In pair in the cell (within a 6 Å In-In distance). To establish bonding between an oxygen atom and its two In neighbors, and hence to determine whether the oxygen is shared between the two In atoms, the contribution to the exponential term of Eq. (2) is evaluated for each In-O bond. To account for possible weak bonds and strong polyhedral distortions caused by disorder in amorphous oxides, the minimum contribution from an In-O bond for the bond to be considered in sharing calculations is set to 0.05, which is three times smaller than the minimum contribution to the ECN from the longest In-O bond in crystalline In_2O_3 with bixbyite structure, 0.15. As an example, the smallest contribution to ECN from an In-O bond to be accounted for in a corner-shared connection in amorphous $In_{54}O_{76}$ with the smallest oxygen content is found to be 0.06, which corresponds to the In-O distance of 2.70 Å, given that the minimum and average In-O distances are 2.14 and 2.16 Å, respectively, and the resulting ECN value is 3.14 for this In atom. Of course, both l_{min} and l_{av} are unique for each In atom in amorphous cells.

Next, each of the 60 atomic configurations obtained from the *ab initio* MD liquid quench simulations was optimized within DFT using the PBE functional. For the optimization, a cutoff energy of 500 eV and a $4 \times 4 \times 4$ Γ-centered k-point mesh were used; the atomic positions were relaxed until the Hellmann-Feynman force on each atom was below 0.01 eV/Å. Finally, the electronic and optical properties of the PBE-optimized amorphous In_2O_{3-x} structures were calculated using the hybrid Heyd-Scuseria-Ernzerhof (HSE06) approach [65,66] with a mixing parameter of 0.25 and a screening parameter α of 0.2 Å^{-1}. Note that only the electronic self-consistent calculations were performed in HSE06, whereas the atomic positions were not relaxed further in HSE06. For each of the 60 realizations, total energy, density of states, electronic band structure, and charge-density distributions were obtained. To quantify the localization of the electronic states, the inverse participation ratio (IPR) of an orbital $\Psi_n(\vec{r}_i)$ can be found from *ab initio* density-functional calculations according to the following equation:

$$\text{IPR}(\Psi_n) = N \frac{\sum_{i=1}^{N} |\Psi_n(\vec{r}_i)|^4}{\left| \sum_{i=1}^{N} |\Psi_n(\vec{r}_i)|^2 \right|^2}, \qquad (3)$$

where N is the number of volume elements in the cell, and i is the index of the volume element. IPR calculations help quantify the electron localization as it represents how many states each atomic orbital is distributed over. The higher the IPR value, the stronger the localization is, while a delocalized state with equal contributions from all atoms in the system corresponds to an IPR value of 1.

In addition, Bader charge analysis for each atom [67] was performed for valence and conduction states. We argue that such calculations provide a significantly more accurate description of the electron localization in disordered materials—especially near highly distorted undercoordinated undershared metal atoms where the charge distribution is likely to be nonuniform—as compared to the traditional electronic structure tools such as density-of-states (DOS) calculations or atomic orbital contributions that rely on a fixed cutoff radius around atoms. We believe that this drawback of the DOS calculations is one of the major reasons why progress has been hampered in obtaining a theoretical understanding of amorphous oxide semiconductors.

Here we stress that the HSE approach provides a significant improvement in the description of the electronic properties of metal oxides, not only for accurate band-gap values and optical properties but also for electron localization at the defect states. Specifically, charge trapping in amorphous metal oxides has been associated with low-coordinated ions and elongated metal-oxygen bonds in the amorphous oxide network, and theoretical models of electron polarons and bipolarons have been proposed for several oxides [68]. Therefore, structural relaxation is important in the description of the structure-electronic property relationships. While further atomic relaxation with the HSE method for the 60 disordered 130–138-atom supercells (that are fully relaxed in PBE) is not computationally feasible, we believe that the results of this work are reliable given that (i) a diverse electronic behavior was found in a-In_2O_{3-x}—from shallow, to weakly localized, to deep trap states, each of which is carefully described by
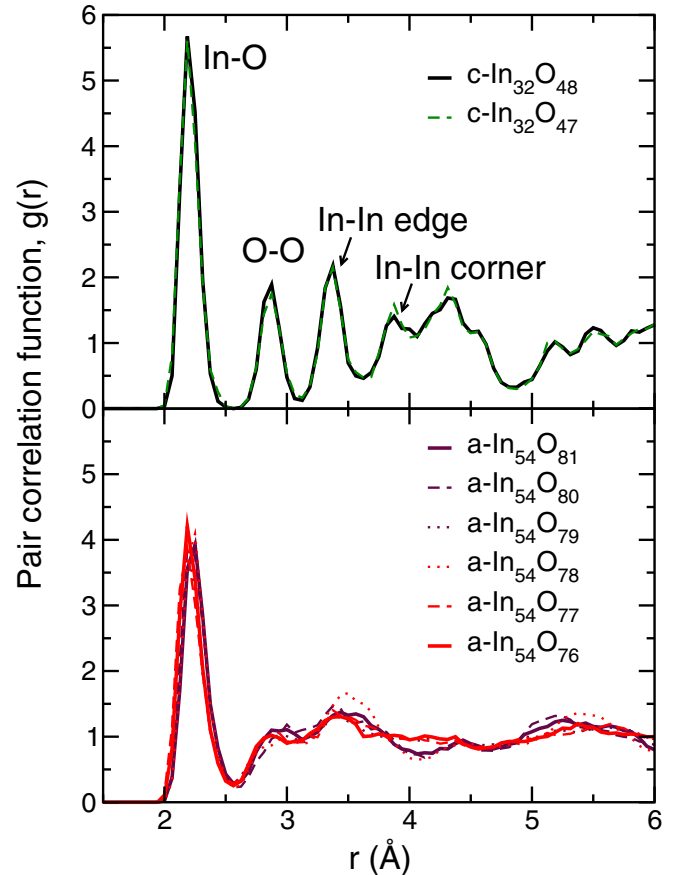

FIG. 2. Pair correlation function in crystalline and amorphous In_2O_{3-x} as calculated from the last 200 MD steps obtained at 300 K for each MD realization. For bixbyite oxide, the first four peaks are labeled. For disordered oxide, each line represents an average of 10 separate MD realizations for the given oxygen stoichiometry.

specific In-In distances and In-O coordination near the defect; and (ii) excellent agreement was found between our theoretically calculated carrier and defect concentrations and those observed experimentally.

Finally, optical absorption was derived from the frequency-dependent dielectric function, $\epsilon(\omega) = \epsilon_1(\omega) + i\epsilon_2(\omega)$, calculated within the independent-particle approximation as implemented in VASP. The imaginary part, $\epsilon_2(\omega)$, is related to the optical absorption at a given frequency ω, and it is determined based on the electronic transitions of the hybrid functional solution. The real part of the complex dielectric function is obtained using Kramers-Kronig relations.

The optimized atomic structures and charge densities were plotted using VESTA software [69].

III. AVERAGE STRUCTURAL CHARACTERISTICS AND DEFECT FORMATION

Figure 2 shows the calculated pair correlation functions for crystalline (bixbyite) and amorphous indium oxides with different substoichiometries. As already mentioned in the Introduction, disorder suppresses not only the structural features beyond the third In shell but also the O-O peak for which $g(r)$ is nearly 1, as has been reported [27,28,39–41]. The
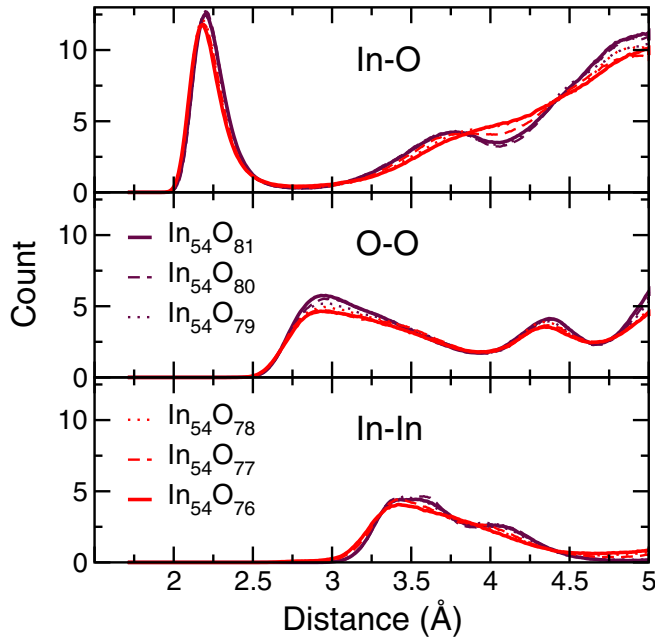
FIG. 3. Distance distributions for In-O, O-O, and In-In pairs in amorphous In_2O_{3-x} calculated using 10 separate MD realizations for each oxygen stoichiometry. The results combine 3000 MD configurations (6 ps) obtained at 300 K for each MD realization, resulting in 30 000 atomic configurations analyzed for each stoichiometry. The results are normalized by the number of MD steps and by the number of realizations, but not by the number of atoms.

TABLE I. The local (first-shell) structural characteristics in amorphous In_2O_{3-x} as calculated from *ab-initio* MD simulations at 300 K. The average distance l_{av}, effective coordination number (ECN), and polyhedra distortion σ^2 are calculated for both In and O atoms. Each value is an average over 3,000 MD steps (6 ps) at 300 K, In(O) atoms in the cell, and over 10 MD realizations for each stoichiometry. The average defect formation energy calculated according to Eq. 4 based on DFT-HSE results is given as an average over 10 realizations for each stoichiometry.

		In-O		O-In		Defect formation
	l_{av} (Å)	ECN	σ^2 (Å^2)	ECN	σ^2 (Å^2)	energy (eV)
a-$In_{54}O_{81}$	2.20	5.37	0.0135	3.60	0.0137	
a-$In_{54}O_{80}$	2.20	5.34	0.0128	3.62	0.0132	−1.75
a-$In_{54}O_{79}$	2.20	5.25	0.0131	3.61	0.0131	+0.45
a-$In_{54}O_{78}$	2.19	5.15	0.0139	3.59	0.0135	+0.93
a-$In_{54}O_{77}$	2.19	5.09	0.0134	3.59	0.0133	+0.13
a-$In_{54}O_{76}$	2.19	5.00	0.0144	3.56	0.0140	+0.25

first peak in the distribution that corresponds to In-O distance is well developed and separated by a pseudogap, implying that amorphous structure has developed in all In_2O_{3-x}. As the oxygen substoichiometry increases, the first peak shifts slightly toward the shorter distances, whereas the medium- and long-range features continue to decrease, signifying that disorder increases for lower O content. The changes in the total distribution function are minimal, hence they may not be captured experimentally. To the best of our knowledge, measurements of the radial distribution function for amorphous In_2O_x as a function of oxygen content are not available in the literature, whereas published works on the structure of amorphous indium oxide often do not report density and/or stoichiometry, making a comparison with theory challenging.

The In-O, In-In, and O-O distance distributions for amorphous In_2O_{3-x} obtained from MD simulations at 300 K are shown in Fig. 3. A reduction in oxygen stoichiometry slightly shifts the first-shell In-O peak toward shorter distances and also suppresses the features at the longer distances, suggesting an increase in disorder. In the O-O distance distribution, Fig. 3, the main changes are found for the O-O distances from 2.8 to 3.2 Å, suggesting that oxygen reduction suppresses the number of O-O pairs near the middle of the soft peak, i.e., the highest-occurring O-O distances, while maintaining the width in the distribution. Since the O-O distances represent the edges in the In-O polyhedra, the results imply stronger deviations from the regular (e.g., octahedral) In-O polyhedra and that the local disorder increases as the oxygen content decreases. The suppressed O-O peak is characteristic for the post-transition-metal oxides with weak metal-oxygen

bonding, ionic in nature [28], where the spherical *s*-orbitals of the In atoms are indifferent to the distortions in the In-O polyhedra [70]. In contrast to the O-O distances, the In-In distribution shifts toward shorter In-In distances with oxygen reduction, Fig. 3. The In-In distance distribution represents the medium-range structure, i.e., how the neighboring In-O polyhedra are shared with each other. While the edge- or corner-sharing correspond to a specific In-In distance in crystalline In_2O_3, namely 3.4 or 3.8 Å, respectively, oxygen reduction broadens the distribution and completely erases the distinction between the edge- and corner-sharing peaks, Fig. 3. Moreover, the presence of short In-In distances, e.g., comparable to 3.26 Å found in elemental In with tetragonal $I4/mmm$ structure, is likely to correspond to a metallic bond formation if a lack of oxygen between the two In atoms allows for direct In-In bonding.

The average In-O bond length, effective coordination number (ECN), and polyhedra distortion σ^2 were calculated next. The statistical averages of these three characteristics are given in Table I for both In and O atoms. Among them, only the coordination numbers show a clear trend with oxygen stoichiometry, with most pronounced changes found for the In-O coordination, which decreases by almost 7% from the stoichiometric case, a-$In_{54}O_{81}$, to a-$In_{54}O_{76}$. Figure 4(a) shows the average ECN(In) for each of the 10 realizations at different oxygen stoichiometry. The differences between the realizations are largest for a-$In_{54}O_{77}$ and a-$In_{54}O_{78}$, suggesting a diverse coordination morphology is at play for this range of oxygen content. While the decrease in the In-O coordination with oxygen reduction is expected, we find that it is not accompanied by a commensurate change in the average In-O distance. More intriguingly, the polyhedra distortion (σ^2) that measures the deviation of individual In-O distances from the average value in a given polyhedra decreases when the oxygen content is slightly reduced from the perfect stoichiometric case, Table I. It has been argued that the reduction of the average polyhedra distortion in a-$In_{54}O_{80}$ is likely to signify that the small substoichiometry helps alleviate the internal strain in the amorphous oxide [29]. Here we find
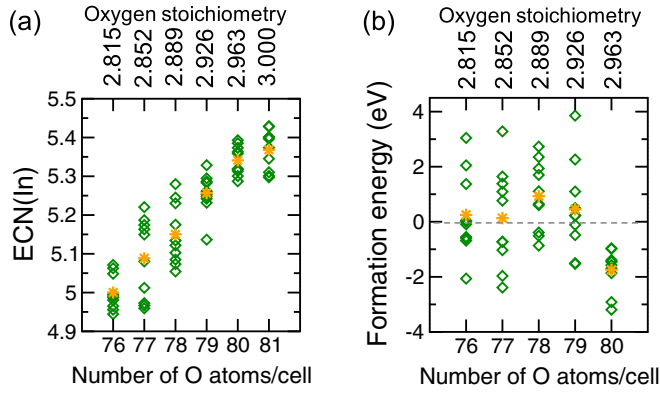
FIG. 4. (a) The effective coordination number (ECN) for the first shell (In-O) in amorphous In_2O_{3-x} as calculated from *ab initio* MD simulations at 300 K. Each value is an average over 3000 MD steps (6 ps) at 300 K and the number of In atoms in the cell; diamonds represent the average for each of the 10 MD realizations for each stoichiometry, while stars represent the average over the 10 MD realizations. (b) Defect formation energy in amorphous In_2O_{3-x} calculated from DFT-HSE approach according to Eq. (4) with O-poor conditions. For each oxygen stoichiometry, the calculations are performed for the structures obtained from 10 MD realizations followed by the structural relaxation in DFT-PBE (diamonds). Stars represent the average over the 10 MD realizations at a given stoichiometry.

that further reduction in oxygen stoichiometry recovers the strong distortion values for both In and O polyhedra, Table I. While σ^2 for In and O become highest in a-$In_{54}O_{76}$, i.e., in the structure with the largest nonstoichiometry, the calculated average distortion for all other In_2O_{3-x} considered in this work is comparable to that in the perfectly stoichiometric case, Table I. The results show that the amorphous indium oxide structures tend to maintain the average local distortion even when the oxygen defect concentration reaches as high as 2.3×10^{21} cm^{-3} (which corresponds to the oxygen nonstoichiometry of $In_{54}O_{77} = In_2O_{2.852}$). This implies that changes in the medium-range structure, i.e., in the way in which the In-O polyhedra are connected with each other to form the network, must occur in response to the oxygen reduction.

The lowest average polyhedra distortion in a-$In_{54}O_{80}$ correlates with the lowest defect formation energy calculated from the DFT-HSE approximation for the substoichiometric cases with respect to the average energy of the structure with higher stoichiometry by one oxygen atom per cell:

$$\Delta E_{\text{defect},i}(\mu) = E_i(In_{54}O_{n-1}) - E_{\text{av}}(In_{54}O_n) + \mu, \quad (4)$$

where μ is the oxygen chemical potential, n stands for the number of oxygen atoms in the cell, and the index i represents different MD configurations. Figure 4(b) shows the defect formation energy for all substoichiometric cases, while Table I lists the same energy values averaged over 10 MD realizations. Using oxygen-poor conditions, we find that ΔE_{defect} is negative in all 10 realizations for a-$In_{54}O_{80}$, and, on average, the defect formation energy is -1.75 eV for this case, suggesting that the formation of oxygen defects in slightly substoichiometric amorphous indium oxide is highly favorable. Although on average the formation of oxygen defects becomes less favorable for higher oxygen nonstoichiome-
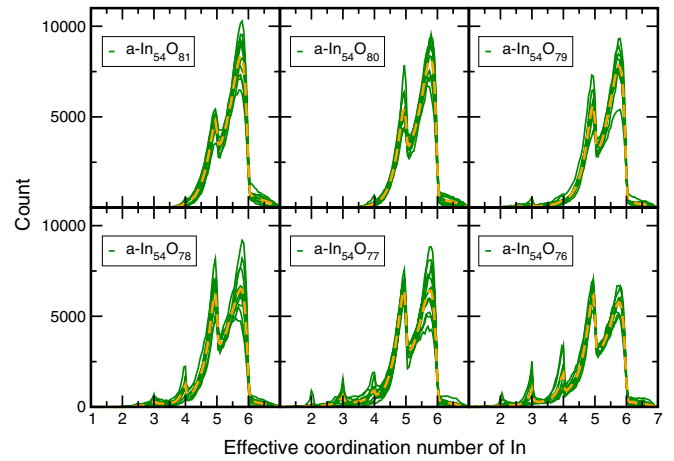

FIG. 5. Distribution of effective coordination numbers (ECNs) of In atoms with oxygen for 10 MD realizations in each amorphous In_2O_{3-x}. The results are based on 3000 MD configurations (6 ps) obtained at 300 K during equilibration step. The dashed orange lines are an average of the 10 MD simulations for each oxygen stoichiometry.

tries, many configurations have negative ΔE_{defect} at each stoichiometry considered in this work, Fig. 4(b). Therefore, the amorphous indium oxide structure can accommodate large defect concentrations by adjusting its local structure and morphology. Both are discussed in great detail in the next sections.

IV. In-O COORDINATION DISTRIBUTIONS AND LOCAL CHARACTERISTICS OF In-O POLYHEDRA

To determine the cause of the decreasing average ECN of In atoms with oxygen reduction, the effective coordination number histograms are plotted for all MD realizations for each In_2O_{3-x}, Fig. 5. The results reveal that, on average, the number of fully coordinated In atoms (ECN > 5.5) decreases only slightly in a-$In_{54}O_{80}$ (48.6%) and a-$In_{54}O_{79}$ (45.1%) as compared to the stoichiometric case, a-$In_{54}O_{81}$ (50.5%). This implies that the amorphous indium oxide structure can accommodate oxygen defect concentrations of up to 11.5×10^{20} (which corresponds to an oxygen stoichiometry of $In_2O_{2.926} = In_{54}O_{79}$) while maintaining the number of fully coordinated In atoms. In a-$In_{54}O_{80}$, the second peak in the coordination distribution (ECN < 5.0) begins to develop, whereas a-$In_{54}O_{79}$ features a notable fraction of severely undercoordinated In atoms with ECN 3.0 in a few MD realizations, Fig. 5. It has been shown that even a small fraction of undercoordinated In atoms may affect the carrier generation and transport properties of the oxides due to the formation of highly localized deep trap states [29]. The binding energy and the degree of electron localization associated with the defects are determined by the spatial distribution of the undercoordinated In atoms, e.g., their proximity with each other. For a-$In_{54}O_{79}$, the probability of the In atoms with severe undercoordination is low, and only a few MD realizations result in clustering of such In atoms [29].

Further reduction of oxygen content leads to a significant decrease in the number of fully coordinated In atoms with ECN > 5.5, specifically to 38.5% in a-$In_{54}O_{78}$, 37.5% in a-$In_{54}O_{77}$, and 34.0% in a-$In_{54}O_{76}$. Therefore, the

undercoordinated In atoms become the majority species, with the heights of the peaks in the distribution function at ECN 4.9, 4.0, and 3.0 steadily increasing as the oxygen content decreases. Our results predict a transition for oxygen defect concentrations between 11.5×10^{20} and 17.2×10^{20} cm^{-3}, i.e., from around $In_2O_{2.926}$ to $In_2O_{2.889}$. Within this range of oxygen stoichiometries, the In coordination morphology is expected to change dramatically, having an effect on the carrier mobility [71,72], as discussed in the sections below. It must be noted here that individual MD realizations have different ECN distributions for all considered values of oxygen stoichiometry, Fig. 5. This is in accord with the largest differences in the average ECN(In) values for each realization in a-$In_{54}O_{78}$ and a-$In_{54}O_{77}$, Fig. 4(a). The realization differences point out that a diverse coordination morphology is possible when the undercoordinated In atoms prevail. This is also supported by the wide distribution in the formation energy in highly nonstoichiometric oxides, Fig. 4, and signifies that a single MD calculation may yield misleading conclusions, highlighting the importance of statistical validation of the results, as is done in this work.

Next, we analyze how the changes in the effective coordination numbers of In correlate with the In-O distances and distortions in the In-O polyhedra. For this, the time-average ECN for every In atom in the cell is calculated as a function of the time-average distortion of that In atom, Fig. 6(a), or as a function of the time-average In-O distance of that In atom, Fig. 6(b). Each point in the plots represents a time average obtained from MD simulations at 300 K for 3000 steps (6 ps) by calculating the corresponding values for each individual In atom in every configuration and then averaging over the 3000 MD configurations. Comparing a-$In_{54}O_{81}$ and a-$In_{54}O_{80}$, the differences in the ECN and σ^2 distributions are almost negligible, with the exception of a reduced number of the fully coordinated In (ECN > 5.5) that have large distortions (σ^2 > 0.02) in the nonstoichiometric case. Independent of the In coordination values, the overall fraction of highly distorted polyhedra (σ^2 > 0.02) decreases from 10.6% in a-$In_{54}O_{81}$ to 8.3% in a-$In_{54}O_{80}$. This substantiates the smaller average distortion in the latter case, Table I, where a small reduction in oxygen content helps suppress the number of strongly distorted In polyhedra, leading to a more uniform amorphous structure.

At larger oxygen substoichiometries, i.e., for a-$In_{54}O_{79}$, a-$In_{54}O_{78}$, a-$In_{54}O_{77}$, and a-$In_{54}O_{76}$, the number of fully coordinated In atoms continues to decrease, Fig. 6. At the same time, the number of undercoordinated In atoms (ECN < 4.0) steadily increases with oxygen reduction. On average, the distortion of In-O polyhedra increases, Table I, and the fraction of highly distorted polyhedra (σ^2 > 0.02) for all In atoms (independent of their coordination) increases to as much as 18.5% in a-$In_{54}O_{76}$. Interestingly, the distortion distribution for the severely undercoordinated In atoms (ECN < 4.0) covers the entire range of values, with nearly equal fractions of weakly (σ^2 < 0.02) and strongly (σ^2 > 0.02) distorted In-O polyhedra, Fig. 6. The wide distribution of both the In coordination numbers and the In-O distortions, Fig. 6, is a result of weak ionic In-O bonding as well as the spherical symmetry of the In $5s^0$ state—both make In atoms indifferent to the exact positions of the oxygen neighbors.
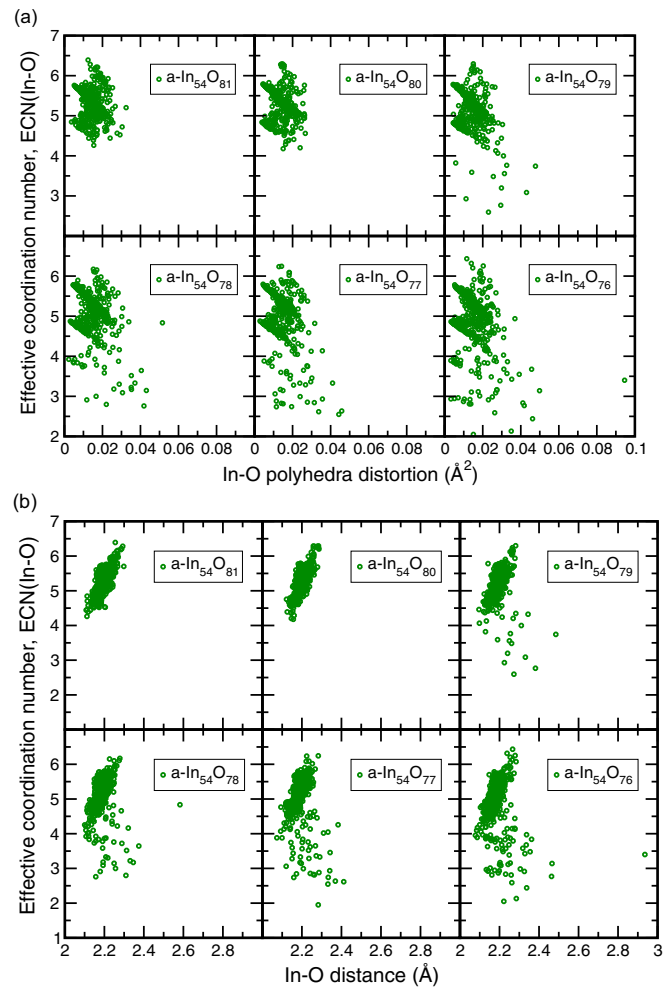

FIG. 6. The average effective coordination number (ECN) for individual In atoms in the amorphous In_2O_{3-x} (a) as a function of the time-average distortion of the In atom; and (b) a function of time-average In-O distance of the In atom. Every data point represents a time average over 3000 MD configurations (6 ps) obtained at 300 K. For each oxygen stoichiometry, the results of 10 separate MD realizations are shown.

In the ionic materials, a reduction in metal coordination numbers is usually accompanied by a shorter M-O bond length. Indeed, the majority of In atoms follow a well-defined dependence of ECN on the In-O distance with the same characteristic slope, Fig. 6(b). However, a notable fraction of low-coordinated In atoms (ECN < 5.0) does not follow the trend, having longer In-O distances than those for In with higher coordination. It has been shown for stoichiometric a-$In_{54}O_{81}$ that longer In-O distances than those that are expected based on the coordination number of a specific In atom lead to charge-density accumulation at the In atom and, consequently, larger electronic contributions from the In atom to the conduction states as compared to other In atoms with close-to-average In-O distances [29]. When the concentration of the In atoms with longer-than-expected In-O distances increases, the spatial distribution of such In atoms, i.e., their clustering or chain formation versus random distribution within the cell, will govern the energy location and the degree of the electron
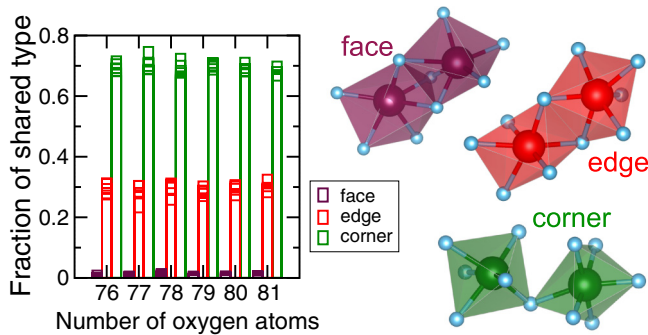
FIG. 7. Fraction of face-, edge-, and corner-shared In-In pairs calculated for 10 separate realizations for each oxygen stoichiometry for amorphous In_2O_{3-x}. The sharing-type pairs have been calculated based on the atomic coordinates of the 3000 MD configurations (6 ps) obtained at 300 K. Examples of the face-, edge-, and corner-shared polyhedra are also shown.

localization of the associated states and hence will determine the resulting transport properties.

We would like to stress here that capturing the structural characteristics of individual In atoms is key to understanding the unique electronic and transport properties of the amorphous indium oxide. The presence, concentration, and spatial distribution of the In atoms with severe under-coordination or with strong distortion or atypical bond lengths cannot be captured with traditional techniques for the structural characterization of amorphous materials, making the defects invisible [73]. Therefore, *ab initio* MD simulations provide valuable information, suggesting that oxygen defects in amorphous indium oxide are likely to originate from the distribution outliers, cf., Fig. 6, while their specific structural characteristics may help understand the resulting differences in the formation and binding energies as well as the electronic properties of the defects and their effect on the overall transport properties of the oxide materials.

V. In-O POLYHEDRA SHARING AND COORDINATION MORPHOLOGY

The reduction on In coordination and the increasing fraction of undercoordinated In atoms at lower oxygen content will affect the medium-range structure, i.e., how the In-O polyhedra are connected with each other. In bixbyite In_2O_3, each In atom shares two oxygen atoms with six In neighbors at In-In distance of 3.4 Å and also shares an oxygen atom with six other In atoms at an In-In distance of 3.7 Å. These polyhedra connections are called edge- and corner-shared, respectively. Compared to the equal fractions of corner- and edge-shared pairs for each In atom in crystalline In_2O_3, disorder reduces the number of edge-shared In-In pairs to about 30% in a-$In_{54}O_{81}$, a-$In_{54}O_{80}$, and a-$In_{54}O_{79}$, as shown in [29]. Here we find that although the statistical variation between the 10 MD realizations for each stoichiometry may be as large as 10%, on average, the same 30:70 ratio is maintained in highly nonstoichiometric structures, Fig. 7, suggesting that the overall polyhedral structure is not affected by the oxygen reduction. Note that the amount of face-shared In-In pairs is small and remains about 1.5% on average in all struc-

TABLE II. The number of face-, edge-, and corner-shared In-In pairs along with the total number of shared In-In pairs in amorphous In_2O_{3-x}. The values represent an average over 10 realizations and 3000 MD configurations (6 ps) for each oxygen stoichiometry. The largest value in each category is highlighted in bold.

	Face	Edge	Corner	Total
a-$In_{54}O_{81}$	**5.73**	**105.94**	238.42	350.09
a-$In_{54}O_{80}$	5.42	102.74	243.26	**351.42**
a-$In_{54}O_{79}$	4.88	98.38	**245.36**	348.62
a-$In_{54}O_{78}$	5.28	100.28	232.96	338.52
a-$In_{54}O_{77}$	4.33	94.38	238.86	337.57
a-$In_{54}O_{76}$	4.24	96.46	229.66	330.35

tures. Face-shared In-In connections (with three oxygen atoms shared by the In neighbors) do not occur in bixbyite In_2O_3, hence they can be considered a structural defect caused by amorphization. Such defects, however, do not result in localized states in the band gap or near the Fermi level: although the In-In distance for the face-shared pair is shorter (about 3.18 Å) than that in elemental In (3.26 Å in tetragonal In with $I4/mmm$ structure), the face-shared In-In pairs cannot produce an In-In metallic bond because the oxygen atoms in the vicinity capture the $5s$ electrons from In to form the ionic In-O bonds, which are stronger than the metallic In-In bond.

While the fractions of differently shared polyhedra do not appear to change with stoichiometry, Fig. 7, an interesting insight is gained from comparing the numbers of face-, edge-, and corner-shared In-In pairs as a function of oxygen content, Table II. We find that the amounts of face- and edge-shared pairs decrease with decreasing oxygen content, however the reduction is not monotonic, with a notable deviation at a-$In_{54}O_{78}$. In marked contrast, the number of corner-shared In-In initially increases, reaching the highest value in a-$In_{54}O_{79}$. As a result, the largest number of total shared In-In pairs is found in a-$In_{54}O_{80}$. This implies that in addition to face-to-edge and edge-to-corner transformations caused by a reduction in oxygen content, there are a few corner-shared pairs created, increasing the total number of shared In-In. These additional corner-shared pairs are likely to form due to longer bond distances and stronger distortions in the In-O polyhedra. We believe that these structural adjustments in the medium-range polyhedral morphology help maintain the number of fully coordinated indium in a-$In_{54}O_{80}$ and a-$In_{54}O_{79}$ with respect to perfectly stoichiometric a-$In_{54}O_{81}$, as discussed in Sec. IV. When the oxygen content decreases further, the lack of oxygen cannot be sustained by an additional reduction in the number of shared pairs; instead, the structure undergoes a coordination transformation characterized by a significant drop in the number of fully coordinated In between a-$In_{54}O_{79}$ and a-$In_{54}O_{78}$ (see Sec. IV). Interestingly, the coordination transformation is accompanied by a slight increase in the number of face- and edge-shared connections in a-$In_{54}O_{78}$, which is followed by an increased number of corner-shared pairs in a-$In_{54}O_{77}$, likely due to the similar face-to-edge and edge-to-corner transformations that occur at higher oxygen content, Table II. Thus, the results imply that the network morphology undergoes several subtle
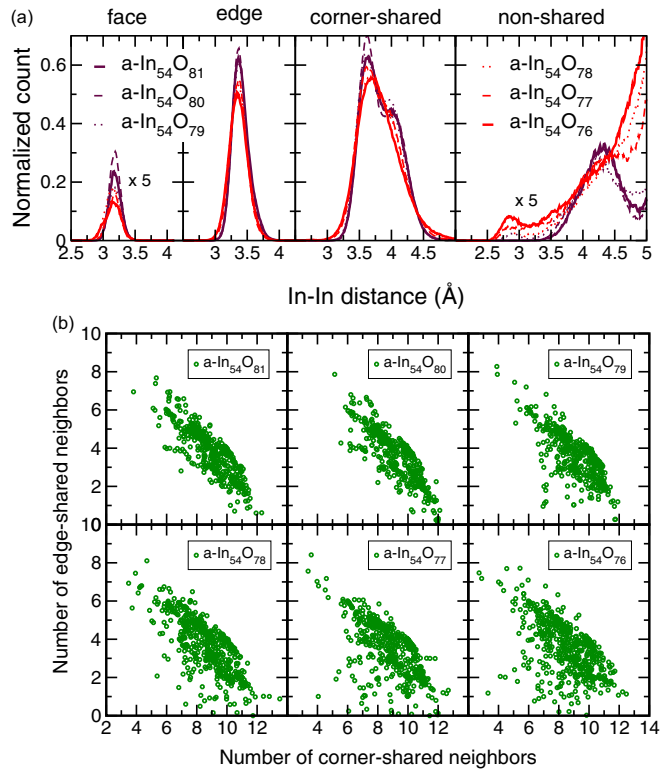
FIG. 8. (a) Distribution of face-, edge-, corner-, and nonshared In-In pairs as a function of In-In distance in amorphous In_2O_{3-x}. The type of sharing is determined based on the number of oxygen atoms that contribute to ECN of both In atoms. The results are based on 3000 MD simulations (6 ps) at 300 K and include 10 MD runs for each a-In_2O_{3-x}. (b) The number of edge-shared In neighbors as a function of the number of corner-shared In neighbors for every In atom in the cell in amorphous In_2O_{3-x}. Every data point represents a time average over 3000 MD configurations obtained at 300 K. The results of 10 separate MD realizations in each stoichiometry case are shown.

TABLE III. The average In-In distance in Å for face-, edge-, and corner-shared In-In pairs in amorphous In_2O_{3-x}. The values represent an average over 10 realizations and 3000 MD configurations (6 ps) for each oxygen stoichiometry.

	Face	Edge	Corner
a-$In_{54}O_{81}$	3.181	3.397	3.801
a-$In_{54}O_{80}$	3.183	3.387	3.830
a-$In_{54}O_{79}$	3.174	3.382	3.819
a-$In_{54}O_{78}$	3.143	3.359	3.821
a-$In_{54}O_{77}$	3.172	3.365	3.807
a-$In_{54}O_{76}$	3.148	3.360	3.812

pairs with short distances implies that metallic bond formation becomes possible—due to the lack of oxygen in the vicinity. It will be shown below that metallic In-In bonds may result in electron localization and deep defect formation for isolated In-In pairs, or they may cause an insulator-to-metal transition when the concentration of such metallic In-In pairs and the probability for their clustering increases upon oxygen reduction.

Now, we compare our results to the recent high-energy, wide-angle x-ray diffraction measurements for amorphous indium oxide [41]. In this work, fitting of the grazing-incidence pair distribution function (PDF) produced three In-In peaks at 2.69, 3.28, and 3.72 Å, assigned to face-, edge-, and corner-shared In-In pairs, respectively. Our theoretical results are in agreement with the edge- and corner-shared In-In distances; the larger calculated values may be attributed to the differences in density (7.1 g/cm^3 in our work versus 4.6 g/cm^3 in experiment [41]). However, the average face-shared distances (3.14–3.18 Å) are notably longer than the observed first In-In peak at 2.69 Å, although the shortest face-shared distance in our calculations was found to be 2.60 Å in a-$In_{54}O_{76}$. Importantly, our results suggest that the presence of nonshared In-In pairs with comparable distances (within 2.5–3.5 Å) and comparable concentration to that of face-shared In-In, Fig. 8(a), is likely to be the reason for the large first In-In peak in experimental PDF as compared to edge- and corner-shared peaks.

In Fig. 8(b), the number of edge-shared neighbors is plotted as a function of the corner-shared neighbors for individual In atoms in all amorphous In_2O_{3-x}. As mentioned above, each In atom in bixbyite In_2O_3 has 12 In neighbors: 6 of them are edge-shared and 6 are corner-shared with the given In atom. It is obvious that disorder has a tremendous effect on the polyhedra sharing: even the perfectly stoichiometric a-$In_{54}O_{81}$ structure has only 17 In atoms among 10 MD realizations, i.e., out of 540 In atoms, that possess 6 edge- and 6 corner-shared neighbors. The average In atom in a-$In_{54}O_{81}$ has 3.9 edge-shared and 8.8 corner-shared neighbors, while the outliers in the overall distribution may have 7 edge-shared and 5 corner-shared In neighbors or only 1 edge-shared and 12 corner-shared neighbors. Oxygen nonstoichiometry has little effect on the average In atoms, but it results in the appearance of severely undercoordinated In atoms, i.e., those with low numbers of both edge- and corner-shared In neighbors. Interestingly, the appearance of a few undercoordinated In atoms

structural transformations when oxygen content decreases. These changes may have a pronounced effect on the electronic and transport properties of amorphous indium oxide.

Figure 8(a) shows the In-In distance distribution calculated for face-, edge-, corner-, and nonshared pairs in amorphous In_2O_{3-x}. For each stoichiometry, the results are averaged over 10 MD realizations. We find that the edge-shared distribution peak is at 3.36 Å in all cases except for a-$In_{54}O_{76}$, where the peak shifts to 3.34 Å. The majority of corner-shared In-In pairs have a distance of 3.6 Å and an In-O-In angle of 110°, while the second soft shoulderlike peak at 4.1 Å corresponds to In-O-In angles of 130°. The corner-sharing distribution widens with oxygen reduction and loses the double-peak nature in a-$In_{54}O_{77}$ and a-$In_{54}O_{76}$, Fig. 8(a). The calculated average distances for face-, edge-, and corner-shared In-In pairs are given in Table III. As discussed above, the total number of shared In-In pairs decreases steadily starting from a-$In_{54}O_{79}$ and continuing for higher oxygen substoichiometry, Table II. The reduction signifies that the number of nonshared In-In pairs that have distances below 4.5 Å increases with oxygen reduction, Fig. 8(a). The presence of nonshared In-In

(1–2 edge-shared and 7 corner-shared neighbors) in a-In$_{54}$O$_{79}$ seems to be compensated by an increased number of overco-ordinated In atoms (7–8 edge-shared and 4–6 corner-shared neighbors), Fig. 8(b). This suggest that the amorphous oxide structures may feature intricate coordination morphology. The fraction of severely undercoordinated In atoms continues to increase significantly in a-In$_{54}$O$_{78}$, a-In$_{54}$O$_{77}$, and a-In$_{54}$O$_{76}$. Moreover, a general trend—the lower the number of edge-shared neighbors, the higher the number of corner-shared neighbors—can be seen in structures with higher oxygen content, i.e., in a-In$_{54}$O$_{81}$, a-In$_{54}$O$_{80}$, and a-In$_{54}$O$_{79}$. As the oxygen content decreases, the overall distribution along this trend broadens significantly, which suggests an increased dis-order for the medium range. Such a level of disorder in the In-O polyhedra network is remarkable given the fact that the density of the structures is only 1% below the crystalline value. This highlights the ability of ionic amorphous oxides to withstand large oxygen nonstoichiometry by adjusting the sharing of In-O polyhedra in the entire cell.

VI. ELECTRONIC PROPERTIES

The calculated density of states (DOS) for fully relaxed structures of amorphous In$_2$O$_{3-x}$, Fig. 9(a), shows that the stoichiometric a-In$_{54}$O$_{81}$ case corresponds to an insulator with a direct band gap at the Γ point of 1.64 eV on average over 10 realizations, each obtained from HSE06 calculations. The value of the band gap ranges from 1.49 to 1.79 eV among the realizations, representing some sensitivity to the variable average In-O distance in each structure (ranging from 2.205 to 2.223 Å in optimized structures) as well as the differences in the morphology that determine the hybridization in the conduction band and, hence, its width. As expected, the Fermi level shifts into the conduction band in all nonstoichiometric structures. In a-In$_{54}$O$_{80}$, the value of the shift is 1.59 eV on average over 10 realizations; it ranges from 1.50 to 1.64 eV among the realizations. This value of the Fermi level shift is comparable to the Burstein-Moss shift in crystalline trans-parent conducting oxides [70], suggesting that the delocalized nature of the conduction band is preserved upon amorphiza-tion. As the oxygen content decreases, states with low density extend into the band gap (for a-In$_{54}$O$_{79}$) and fill the entire band gap for structures with lower oxygen stoichiometries. To characterize the degree of electron localization of these states, the inverse participation ratio is calculated according to Eq. (4) and given in Fig. 9(b). Most of the defect states within the band gap are highly localized with comparable IPR values to those at the top of the valence band (the origin of the localized states at the top of the valence band has been discussed in detail in [29]). Importantly, the localization of the states near the Fermi level—the states that are responsible for carrier transport as well as electron scattering—increases only moderately, except for a few realizations in the a-In$_{54}$O$_{77}$ case where the electron localization is significant [IPR $\approx$ 10 near E_F, Fig. 9(b)]. Below, the defect states will be analyzed in more detail by identifying individual atoms that are the primary or major contributors to these states and associating the electronic features of the defect states with the structural characteristics of these atoms.
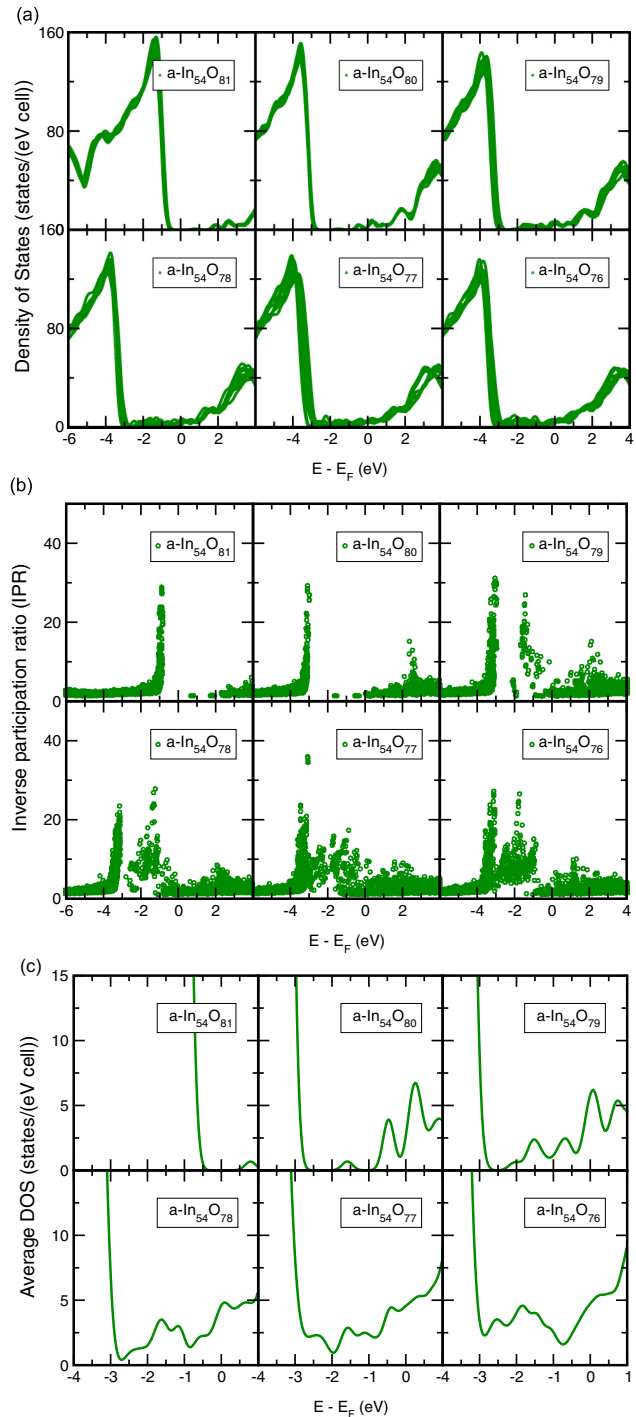

FIG. 9. Calculated (a) density of states (DOS), (b) inverse par-ticipation ratio (IPR), and (c) average DOS for the gap states for amorphous In$_2$O$_{3-x}$. All results are obtained using hybrid functional (HSE06) calculations for the structures optimized using DFT-PBE. In (a) and (b), 10 MD+DFT(HSE) realizations for each oxygen stoichiometry are shown simultaneously, whereas in (c) an average over the 10 realizations is given.

In Fig. 9(c), the average DOS calculated from 10 realizations for each stoichiometry is shown. As discussed in earlier works [28], at low oxygen substoichiometry, the

TABLE IV. The integrated number of states calculated within two energy ranges: from -0.1 to 0.1 eV, which represents free-carrier concentration, and from -2.5 to -1.0 eV, which corresponds to deep defect concentration. Also, the electron velocity calculated along the [111] bandlike state at the energy where the band crosses the Fermi level. The calculations are based on DFT-HSE density of states averaged over 10 realizations for each oxygen stoichiometry, Fig. 9(c).

	Free carriers $(\times 10^{20}$ cm$^{-3})$	Deep defects $(\times 10^{21}$ cm$^{-3})$	Electron velocity $(\times 10^{5}$ m/s$)$
a-In$_{54}$O$_{80}$	3.3		1.39
a-In$_{54}$O$_{79}$	6.6	0.4	1.04
a-In$_{54}$O$_{78}$	5.3	1.2	0.89
a-In$_{54}$O$_{77}$	5.4	1.1	0.58
a-In$_{54}$O$_{76}$	5.6	2.2	0.80

density of states at 0 K features a characteristic gap, the so-called Coulomb gap, near the Fermi level that signifies the formation of chainlike conductivity channels. As the oxygen content decreases, the gap fills up and the DOS remains nearly constant in the vicinity of the Fermi level, as expected for a metal with a uniform charge density distribution. Accordingly, the free-electron concentration, estimated as an integrated DOS within a -0.1 to 0.1 eV energy range, is nearly constant for a-In$_{54}$O$_{78}$, a-In$_{54}$O$_{77}$, and a-In$_{54}$O$_{76}$, Table IV. The highest free-electron concentration is obtained in a-In$_{54}$O$_{79}$. The values are in excellent agreement with the experimental values for amorphous indium oxide grown at an oxygen partial pressure of 1–8 mTorr [28]. In addition, we estimate the concentration of deep strongly localized defect states that are formed within the energy range approximately from -1 to -2.5 eV below the Fermi level, Fig. 9(c) and Table IV. We find that the deep defect content is comparable to that of amorphous In-Ga-Zn-O [32].

The calculated optical absorption for amorphous In$_2$O$_{3-x}$ is shown in Fig. 10. At small oxygen nonstoichiometry (in a-In$_{54}$O$_{80}$), a pronounced Fermi level shift widens the optical window, and the material becomes nearly transparent within the entire visible range. The low absorption is associated with the intraband transitions, i.e., within the half-occupied conduction band formed by delocalized states, case a-In$_{54}$O$_{80}$ in Fig. 9(b). We note here that despite the aforementioned variation in the band-gap values, the optical properties of different MD+DFT(HSE) realizations are similar for 10 cases of stoichiometric a-In$_{54}$O$_{81}$ and also for 10 cases of a-In$_{54}$O$_{80}$. In marked contrast, the optical absorption curves vary significantly for different realizations with lower stoichiometry, due to the presence of defect states with different degrees of electron localization that leads to a different Fermi level shift, Figs. 9 and 10. For example, in a-In$_{54}$O$_{79}$, different realizations yield notably different electronic properties: several realizations result in (i) further Fermi level shift up into conduction states, (ii) further optical band gap widening, and (iii) further increase of the carrier concentration (as signified by a higher Drude peak at about 0.5 eV)—as compared to the cases of a-In$_{54}$O$_{80}$. At the same time, other realizations at this oxygen stoichiometry show a reduction in the optical gap and an increased absorption near 1.5–2.5 eV, Fig. 10. The
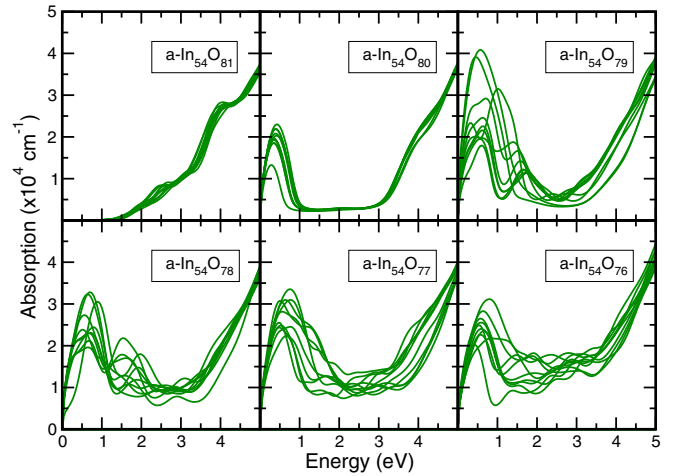

FIG. 10. Calculated optical absorption for 10 MD+DFT(HSE) realizations for each oxygen stoichiometry is shown for amorphous In$_2$O$_{3-x}$. Average over the 10 realizations. All results are obtained using hybrid functional (HSE06) calculations for the structures optimized using DFT-PBE.

latter is associated with the formation of a deep state inside the fundamental band gap, an electron trap. The absorption within the infrared and visible ranges continues to gradually increase with oxygen reduction, leading to a complete transition to metallic behavior found in all realizations in the a-In$_{54}$O$_{76}$ case, Fig. 10. In all structures with oxygen stoichiometry below 2.926 (oxygen defect concentration of 11.5×10^{20} cm^{-3} and above), structural variations associated with the different coordination morphology (i.e., the spatial distribution of the undercoordinated In atoms) will lead to pronounced differences between the realizations, yielding significantly different optical absorption profiles, overall optical transmission, and the total number of free carries. This again highlights the necessity for adequate statistical representation using multiple realizations or significantly larger supercells, since a single calculation in a 100–200-atom cell may produce misleading conclusions.

VII. ELECTRON LOCALIZATION AND STRUCTURE-PROPERTY RELATIONSHIPS FOR METALLIC FORMATIONS

To analyze the localized states that arise in a-In$_{54}$O$_{79}$, a-In$_{54}$O$_{78}$, a-In$_{54}$O$_{77}$, and a-In$_{54}$O$_{76}$, Bader charge contributions from every In atom are calculated for the occupied defect states [located within up to 3 eV below the Fermi level, Fig. 9(b)] and plotted as a function of the effective coordination number of the given In atom, Fig. 11. (Note that here the ECN, effective distance, and distortion values discussed in this section are calculated based on the atomic coordinates in the optimized 0 K structures for which the electronic properties were calculated.) We find that the largest Bader charge contribution to the defect state in each realization is from a low-coordinated In atom, ECN<5. The ECN value calculated as an average over the In coordination of the largest Bader contributor in each of the 10 realizations for different stoichiometry decreases gradually from 3.63 to 3.61, to 3.39, to 3.25 for a-In$_{54}$O$_{79}$, a-In$_{54}$O$_{78}$, a-In$_{54}$O$_{77}$, and a-In$_{54}$O$_{76}$,
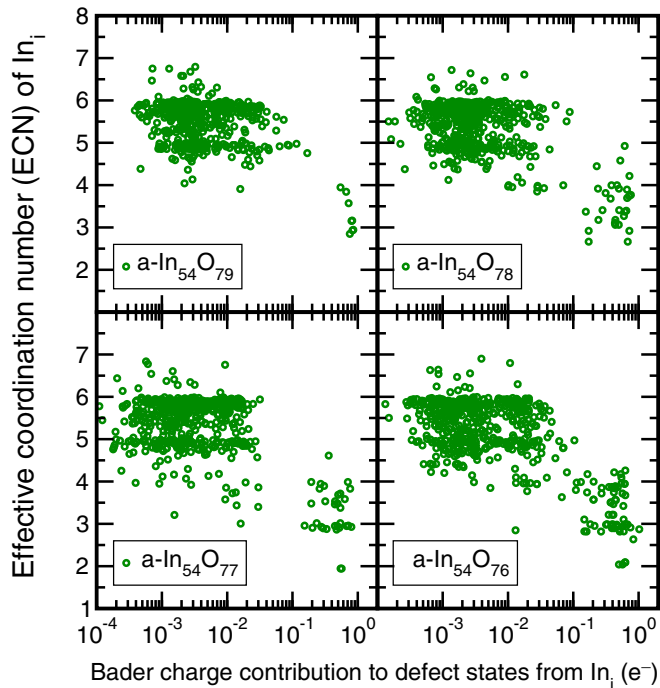
FIG. 11. The effective coordination number of individual In atoms as a function of the Bader charge contributions from the atom to the defect state(s) located in the band gap at up to 3 eV below the Fermi level. Each state holds $2e^-$. All 54 In atoms in each of the 10 supercells are shown for each oxygen stoichiometry; only the largest Bader charge contribution to the defect state(s) for each In atom is shown. The results are obtained using hybrid functional (HSE06) calculations for the structures optimized using DFT-PBE approach.

respectively. This is consistent with the overall decreasing ECN calculated for all In atoms, Table I, and the growing number of In atoms with extremely low coordination, Fig. 6, when the oxygen content decreases. A clear dependence of the charge localization on ECN(In) is observed in a-In$_{54}$O$_{79}$, i.e., for the oxygen stoichiometry of 2.926 and oxygen defect concentration of 11.5×10^{20} cm^{-3}: in this case, the largest Bader charge contributions (about $1e^-$) are associated with the lowest ECN values (ECN<4), whereas the majority of In atoms with high coordination (ECN>4) have low Bader charge contributions to the defect state, namely less than $0.1e^-$, Fig. 11. At lower oxygen content, a broad range of In coordination numbers have a large Bader charge of about 0.5-$1e^-$, namely from ECN=5.0 to 3.5 in a-In$_{54}$O$_{78}$ and from ECN=4.5 to 2.0 in a-In$_{54}$O$_{77}$ and a-In$_{54}$O$_{76}$, Fig. 11. At the same time, an increasing number of severely undercoordinated In atoms (with ECN $\approx$ 4 and ECN $\approx$ 3) have moderate or orders-of-magnitude smaller Bader charge (below $0.1e^-$) as the oxygen substoichiometry increases, Fig. 11. Therefore, the ECN value alone is not a sufficient descriptor to predict the charge localization and, consequently, to explain the deep traps in highly nonstoichiometric amorphous indium oxide. Other structural characteristics of individual In atoms should be considered in combination with ECN in order to predict localized defects.

In addition to ECN, we analyzed the average In-O distance and distortion (or distance variance within a given InO poly-

hedron), cf., Figs. 6(a) and 6(b). Indium atoms with a longer than average In-O distance appear to have larger Bader charge contributions, in agreement with our earlier findings for stoichiometric a-In$_{54}$O$_{81}$ [29]. Specifically, for the In atoms that have a defect Bader charge of $0.2e^-$ or greater, the average ECN, average effective In-O distance, and average distortion are, respectively, 3.46, 2.25 Å, and 0.006 Å^2 in a-In$_{54}$O$_{79}$; 3.63, 2.26 Å, and 0.020 Å^2 in a-In$_{54}$O$_{78}$; 3.28, 2.26 Å, and 0.017 Å^2 in a-In$_{54}$O$_{77}$; and 3.31, 2.27 Å, and 0.019 Å^2 in a-In$_{54}$O$_{76}$. These values differ significantly from the overall structural characteristics in a-In$_2$O$_{3-x}$, Table I. Therefore, not only a small ECN, but also longer than expected effective In-O distances that can be categorized as "outliers" in the ECN-versus-distance plot, Fig. 6(b), as well as larger than usual polyhedral distortions, Fig. 6(a), are the reasons for higher Bader charge values. It must be noted that the distortion considered in this work as the distance variance within a given InO polyhedron does not account for specific symmetry or distribution of the oxygen atoms around the central In, and therefore it is not a reliable parameter. For example, in one of the a-In$_{54}$O$_{76}$ realizations, we find two In neighbors that have similar ECN values of 3.63 and 3.95; a similar average In-O distance of 2.19 and 2.18 Å; and a polyhedra distortion of 0.072 and 0.002 Å^2, respectively, yet their largest Bader charge is $0.02e^-$ and $0.61e^-$, respectively. A closer inspection of the oxygen environments around the In atoms reveals that the strongly distorted polyhedra contain two oxygen atoms at longer-than-expected distances but directed towards the second In, effectively screening the former In atom from the latter, thus reducing its Bader charge. This finding explains the observation that some low-coordinated In atoms have small Bader charge, Fig. 11.

Moreover, the coordination of individual In atoms or a combination of several structural characteristics do not show correlation with the energy of the defect state within the electronic structure. For example, we find that in a-In$_{54}$O$_{76}$, a low-ECN In atom (ECN=2.95, effective In-O distance 2.20 Å, and distortion 0.0026 Å^2) is the largest Bader contributor to a defect state located at −2.3 eV with respect to the Fermi level, i.e., with E_F at zero. At the same time, this realization has a deeper defect located at −3.0 eV, and the largest Bader contribution to this state is from an In atom with a larger ECN, 3.95 (In-O distance 2.18 Å and distortion 0.0016 Å^2). It should be noted that the results also reveal that the Bader charge contributions from individual In atoms do not correlate with how deep the defect state associated with the In atom is, suggesting that further analysis is required.

The mutual distribution of the abundant undercoordinated In atoms must be taken into account in order to explain the degree of charge localization and the resulting diverse electronic properties. First, in addition to In-O coordination, we consider the structural characteristics of next nearest neighbors of the low-coordinated In atoms. Specifically, we find that the largest (above $0.1e^-$) Bader charge contributions in each realization are from In atoms that on average (i.e., among 10 realizations) have ECN $\approx$ 3.5 and also have at least one low-coordinated In neighbor with ECN $\approx$ 4.1 that is located at a short In-In distance of 3.4 Å. These results are in agreement with our earlier findings for the localized states in a-In$_{54}$O$_{79}$ where the energy location of the defect state below the Fermi level was found to

correlate not only with how low the ECN value of an In atom is, but also with how low the ECN value of its undershared In neighbor is and how short the distance between the two In atoms is [29]. In other words, the In-In distance between the two low-coordinated In atoms and whether or not they share oxygen atom(s) are important factors that contribute to the formation of isolated In-In metallic bonds and should be considered to determine the energy location of the associated deep electron traps within the band gap in a-$In_{54}O_{79}$ [29]. It should be noted here that the In-In distance alone, i.e., without taking into account the In coordination, cannot predict the electron localization. First of all, a face-shared In-In pair is a common structural defect in amorphous indium oxide at any oxygen stoichiometry, Figs. 7 and 8(a). As mentioned in Sec. V, the average In-In distance for a face-shared pair is 3.16 Å, while the shortest face-shared distance is found to be 2.60 Å. This is significantly shorter that the In-In distance in metallic elemental In, 3.26 Å. However, the face-shared connections are formed when the two In atoms share three oxygen atoms with each other. The presence of the oxygen atoms effectively screens the In atoms from each other: the formation of the six ionic In-O bonds inhibits a direct inter- action between the In orbitals, i.e., it prevents the formation of a metallic In-In bond. Therefore, face-shared In-In pairs should be excluded from consideration as a cause of electron localization.

In this work, we focus on a combination of low ECN, short In-In distances, and no oxygen sharing between pairs of In atoms in order to study the effect of clustering of increasingly abundant undercoordinated In atoms in highly nonstoichiometric oxides on the formation of deep localized states. To do this, we set the following structural criteria that may allow In atoms to form direct metallic bonds with the In neighbors: for every undercoordinated In atom (ECN<5.2), we find all undercoordinated In neighbors (ECN<5.2) that are at the In-In distance of 4.5 Å or below and do not share any oxygen atoms between them. Here, one should recall that the In-In distance within 3.1–3.8 Å is typical for edge-shared In-In pairs (two oxygen atoms shared the In neighbors), and the In-In distance within 3.3–4.5 Å is typical for corner-shared In-In pairs (one oxygen atom shared by the In neighbors), Fig. 8. Therefore, two In atoms located at a distance of 4.5 Å or below from each other without sharing an oxygen should be examined as a potential nonshared In-In defect that may result in a metallic In-In bond. For comparison, we remind the reader here that the In-In distance in elemental In metal with tetragonal $I4/mmm$ structure is 3.26 Å. Note, the ECN limiting value of $\leqslant 5.2$ may appear quite high since a large fraction of In atoms with coordination of 4.5–5.2 have small Bader charge contributions, below $0.1e^-$, Fig. 11. However, we would like to capture the small fraction of "outliers," the In atoms that have ECN within this range, but contribute within 0.5–$0.6e^-$ to the defect state Bader charge, Fig. 11. We antici- pate that the other structural features—longer-than-usual In-O distances, short In-In distances, and undersharing—will help us capture the important contribution from these "outliers."

First, we calculate the percentage of the In atoms that are nonshared according to the criteria set above: it is 2%, 6%, 13%, 19%, 23%, and 28% in a-$In_{54}O_{81}$, a-$In_{54}O_{80}$, a-$In_{54}O_{79}$, a-$In_{54}O_{78}$, a-$In_{54}O_{77}$, and a-$In_{54}O_{76}$, respectively,
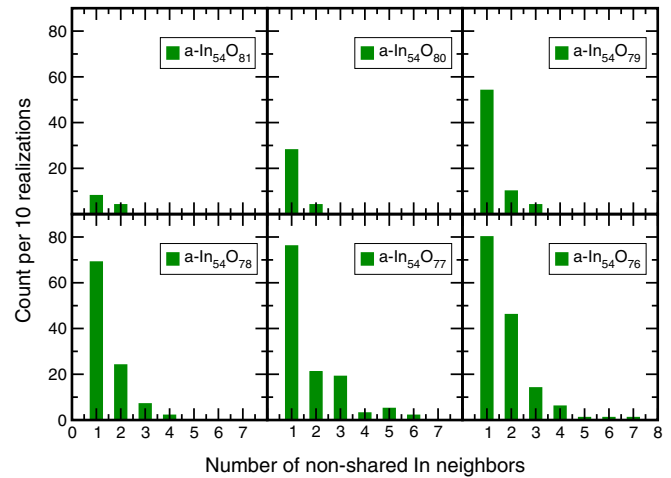

FIG. 12. The number of nonshared In neighbors that are located at the distance of 4.5 Å or below from each other, and both are un- dercoordinated with oxygen (ECN<5.2). The results are calculated based on 10 MD realizations for each oxygen stoichiometry using the amorphous In_2O_{3-x} structures optimized within DFT-PBE. The total number of In atoms within 10 realizations is 540.

out of the total 540 In atoms in 10 MD configurations for each stoichiometry. This means that nearly a third of all In atoms in a-$In_{54}O_{76}$ have at least one In neighbor at the In-In distance below 4.5 Å with which it does not share an oxygen atom. The number of In atoms with a single nonshared In neighbor increases from 8 (in a-$In_{54}O_{81}$) to 80 (in a-$In_{54}O_{76}$), calculated among the 540 In atoms in 10 MD configurations for each stoichiometry, which corresponds to 1.5% and 15%, respectively, Fig. 12. The number of In atoms with 2 or more nonshared In neighbors also increases with oxygen reduction, reaching as many as 7 neighbors found in one realization for a-$In_{54}O_{76}$, Fig. 12. The In atom that does not share any oxygen atoms with 7 In neighbors is illustrated in Fig. 13(a) where the effective coordination numbers and In-In distances to the central In atom are given. Here we must stress an important difference between a-$In_{54}O_{77}$ and a-$In_{54}O_{76}$: the number of two-neighbor nonshared undercoordinated In atoms doubles in the latter case, signifying that at this oxygen stoichiom- etry, the In-In metallic chains become more prevalent and also longer. Indeed, among 10 realizations for a-$In_{54}O_{76}$, we find two configurations where there are only one- and two- neighbor nonshared undercoordinated In atoms. In both cases, the network diagram represents a set of chains that never cross with each other, and one of the chains consists of 7 nonshared undercoordinated atoms with no loops, Fig. 14(a). An even longer chain is found in another configuration for a-$In_{54}O_{76}$ where 11 undercoordinated In atoms are all connected in one single chain, Fig. 14(b). In a-$In_{54}O_{77}$, however, the longest chain consists of 5 undercoordinated nonshared In atoms, and overall the chains are more scarce and shorter. Therefore, the oxygen stoichiometry between a-$In_{54}O_{77}$ and a-$In_{54}O_{76}$ marks the transition to metallic networks with abundant chain- like formations. On the other hand, starlike formations, where the chains cross when the central In atom has more than two neighbors, gradually appear with higher oxygen non- stoichiometry: we find 3-branch stars in a-$In_{54}O_{79}$; 3- and
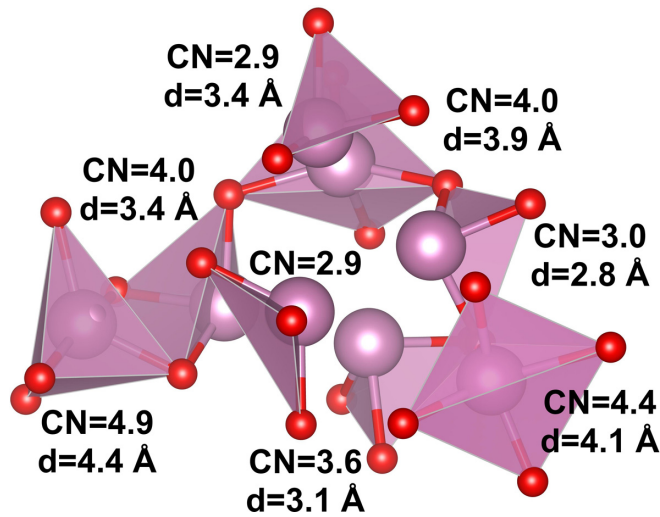
FIG. 13. An In atom that does not share any oxygen atoms with 7 In neighbors. All the In atoms in the cluster have low effective coordination numbers (labeled as CN) and short In-In distances to the central In atom. This example is from one of the 10 MD realizations for a-In$_{54}$O$_{76}$ after structural optimization. The network diagram for the metallic cluster is shown in Fig. 14(c).

4-branch stars in a-In$_{54}$O$_{78}$; 3-, 4-, 5-, and 6-branch stars in a-In$_{54}$O$_{77}$; and 3-, 4-, 5-, 6-, and 7-branch stars in a-In$_{54}$O$_{76}$, Fig. 12. Three characteristic examples of a-In$_{54}$O$_{76}$ configurations with a long chain and no crossing between four different chains, the longest chain with two 4-atom stars and one 3-atom star (giving rise to two loops), and a network with a 7-branch star and multiple interconnected loops are shown in Fig. 14. We note that the structures with higher oxygen content are similar, with the exception of a smaller number of star branches or loops and shorter chains, hence they may be considered as a part of the diagrams shown in Fig. 14.

Among 10 realizations for a-In$_{54}$O$_{76}$, the distribution of the metallic nonshared undercoordinated In pairs is very diverse. In addition to the three examples we show in Fig. 14, we find that other realizations often have several chains that are not connected with each other. In fact, only a single realization results in a single chain with all nonshared undercoordinated In atoms connected, Fig. 14(b). The remaining 9 configurations have 2, 2, 3, 3, 3, 3, 4, 4, and 5 independent chains not connected to each other. Each chain consists of 2 or up to 11 atoms. Four configurations do not have any loops within their chains; another four configurations have 1–3 loops that connect 3–4 In atoms within the chain; and only two configurations have pronounced clustering with 8–9 loops, shown in Figs. 14(a) and 14(c). While an infinite number of distinct atomic configurations should be expected for a disordered structure, it is clear that amorphous indium oxide tends to spread out the individual metallic bonds within the amorphous cell in percolation-like single-atom chain formations. A significant fraction of the realizations for a-In$_{54}$O$_{76}$ do not feature strong metallic clustering. This finding is consistent with earlier results for a-In$_{54}$O$_{80}$ where the oxygen defect is found to be a delocalized shallow donor where the lack of oxygen is shared between as much as a third of In atoms with low coordination (ECN<5.0) instead of resulting in a
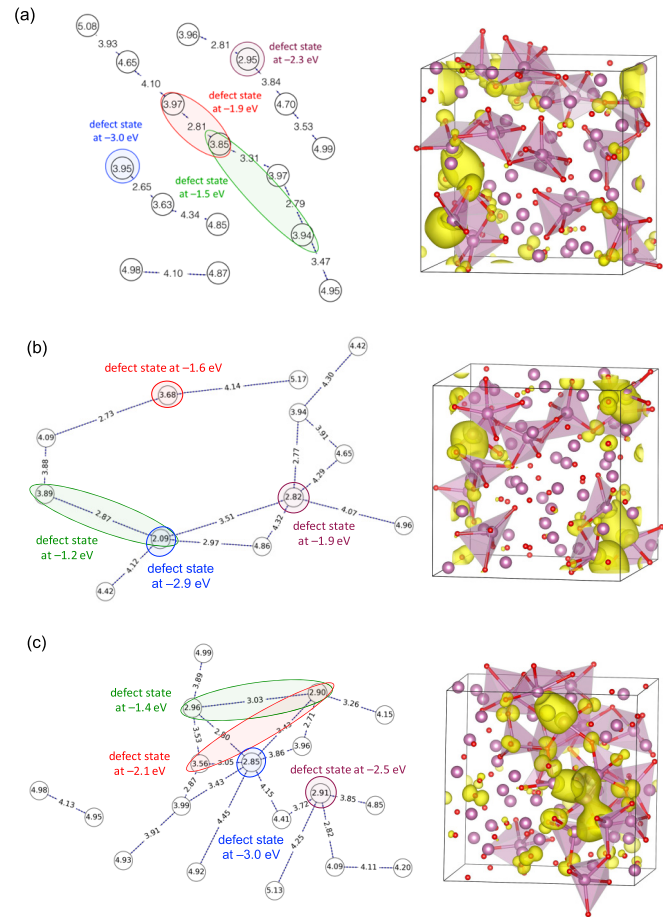

FIG. 14. Schematic representation of nonshared undercoordinated In atoms in three realizations for a-In$_{54}$O$_{76}$ after structural optimization. For the graph plots, only nonshared In-In pairs that consist of In atoms with ECN<5.2 and have the In-In distance below 4.5 Å were selected. Individual ECN values are shown inside the circles, and the In-In distances (in Å) for nonshared connections are shown along the lines. Also, the main contributors (those with the Bader charge of $0.2e^-$ or above) to defect states are highlighted, and the energy of the corresponding defect state with respect to $E_F = 0$ eV is given. In each case, the charge-density distribution calculated for the four defect states is shown on the right.

strongly localized state as in crystalline indium oxide with an oxygen vacancy [29]. The tendency for a more uniform coordination distribution in amorphous indium oxide arises from the weak ionic In-O bonding combined with bond reconfiguration facilitated by the lack of periodicity. The metallic chainlike networks is likely to be the reason for a higher electron velocity in a-In$_{54}$O$_{76}$ as compared to a-In$_{54}$O$_{77}$, Table IV, because such morphology supports percolation for the extended conductivity paths.

Bader charge calculations reveal that 84% of the undercoordinated In atoms (ECN<5.2) with a single nonshared In neighbor (ECN<5.2 and In-In distance below 4.5 Å) among 10 MD realizations of a-In$_{54}$O$_{76}$ contribute below $0.1e^-$ to the occupied defect states located within up to 3 eV below the Fermi level in the conducting oxides, cf., Fig. 9(b). Among the undercoordinated In atoms with two nonshared undercoordinated In neighbors, about 46% have Bader charge

contributions below $0.1e^-$. All undercoordinated In atoms with 3, 4, 5, 6, or 7 nonshared undercoordinated In neighbors contribute more than $0.1e^-$ and up to about $1e^-$ for the most localized state. This finding clearly indicates that clustering is playing an important role in localization. However, above $0.1e^-$, the Bader charge values do not directly correlate with the number of nonshared In neighbors. For example, the In atom with 7 nonshared In neighbors has the largest Bader contribution of $0.27e^-$ to one of the defect states, whereas the two largest Bader charge contributions, $1.03e^-$ and $0.83e^-$, are from In atoms that have only two nonshared undercoordinated In neighbors (note, the examples belong to different realizations).

To understand the relatively low Bader charge on the In atom with 7 nonshared In neighbors, we create a graph plot using the structural criteria set above: we find all In atoms that have low ECN (below 5.2) and are nonshared with other low-ECN In atoms (ECN<5.2) being at the In-In distance below 4.5 Å from each other, and we plot a networklike graph showing the ECN values inside circles to represent undercoordinated In atoms and connecting the atoms that are nonshared using lines that show the In-In distance. The result is shown in Fig. 14(c). We find that the undercoordinated In atom with 7 nonshared In neighbors is part of a cluster of undercoordinated In atoms with similar ECN (2.85, 2.90, 2.96, 3.56, and 3.96) and that several of the nonshared connections within the cluster have similar In-In distances (2.71, 2.80, 3.03, 3.05, 3.43, and 3.53 Å), Fig. 14(c). As a result, the first four In atoms in the cluster have nearly equal Bader charge ($0.27e^-$, $0.42e^-$, $0.38e^-$, $0.44e^-$, and $0.02e^-$, respectively) to the ECN values above. Importantly, the clustering of In atoms with alike coordination at alike nonshared distances is the reason for the defect to be closer to the Fermi level: among three defect states for this realization of a-In$_{54}$O$_{76}$, the given defect is located at −1.4 eV. This is nearly 1 eV higher than the deepest defect for this realization that is located at −2.5 eV and is associated with an In atom that has a Bader charge of $0.75e^-$, the largest value for these configurations. The latter In atom also has a low ECN=2.91 and is nonshared with 4 In neighbors, one of which has ECN=4.09 and is located at the shortest distance of 2.82 Å. However, the other three nonshared In neighbors have higher ECN values, 4.41, 4.85, and 5.13, and are at notably longer distances, 3.72, 3.85, and 4.25 Å, from the given In with the largest Bader charge. This arrangement makes the two In atoms with the lowest ECN isolated, and it leads to stronger localization at the corresponding state associated with the two atoms, Fig. 14(c). For completeness of our analysis, we also consider an intermediate defect state for the same realization. The defect state is located at −2.1 eV below the Fermi level and has the largest Bader charge contribution ($0.44e^-$) from an In atom that has ECN=3.56 and a longer-than-expected In-O distance of 2.22 Å. Although the ECN value is notably higher than those for its two nonshared In neighbors, 2.85 and 2.96, located at 3.05 and 3.53 Å from the given In atom, it has a third nonshared neighbor with ECN=3.99 and located at 2.87 Å. Hence, this state corresponds to a very short In-In nonshared connection between two In atoms with relatively low ECN but surrounded by two In with even lower ECN but at a longer distances. The mixed nature of the ECN and distance values may explain the

intermediate energy location of the defect (−2.1 eV) that is between −2.5 and −1.4 eV. The atoms are part of the complex illustrated in Fig. 14(c). A closer analysis reveals that several of the In atoms in the defect state have their oxygen bonds pointing outward and away from a line connecting the In atoms, thus allowing for direct overlap of the In-$5s$ orbitals that favors the formation of a metallic In-In bond.

The above results help explain why the calculated Bader charge contributions from the In atoms with severe undercoordination, ECN $\approx$ 3 and ECN $\approx$ 2, may be relatively low, below $0.2e^-$ for the state, Fig. 11, and also why the deep defect states may be split by more than 1 eV in energy despite similar ECN values and a similar number of nonshared neighbors for the In atoms associated with each defect. In addition to extreme structural characteristics of individual In atoms when the In-O coordination, In-O and In-In distances, polyhedra distortion, and/or undersharing belong to the tails of the respective distributions, Figs. 6 and 8, one has to take into account the spatial distribution of the "outliers" and their environment, i.e., the structural features of the surrounding In neighbors, in order to explain the resulting charge localization. An isolated under-coordinated In-In pair—the one for which all other In neighbors have significantly higher ECN, share one or two oxygen atoms with the two In atoms, and are at an In-In distance that falls within the corresponding corner- or edge-shared distribution—will result in a deeper electron trap as compared to a cluster that consists of more than two In atoms with similar ECN and similar In-In distances, even if the ECN values are lower and the In-In distances are shorter in the latter case. In other words, the energy location of a defect moves toward the Fermi level as the number of In atoms in a cluster of neighbors with similar low ECN and similar short In-In distances increases. Stronger interaction between alike "outliers" reduces the electron localization of the defect state.

Based on the results for different oxygen stoichiometries, clustering of low-coordinated In atoms is likely to occur in a-In$_{54}$O$_{76}$, a-In$_{54}$O$_{77}$, and a-In$_{54}$O$_{78}$, but not in a-In$_{54}$O$_{79}$, where the undercoordinated In atoms are the minority defects, isolated from each other within the amorphous structure, hence the corresponding states are strongly localized—as evident from the large Bader charges for most of the low-coordinated In atoms (ECN<4.0), Fig. 11, and also from the narrow energy range where the defect states are located, Fig. 9(b). At low oxygen stoichiometries, the increased number of undercoordinated In atoms and broad distribution of their ECN values leads to intricate spatial arrangements of these In atoms, from clustering to rings to percolation-like chains formed by the undercoordinated In atoms with short-distant nonshared connections. Schematic graph plots are employed to illustrate the diverse morphology of undercoordinated nonshared In-In pairs in a-In$_{54}$O$_{76}$. The structure discussed above, Fig. 14(c), has an In atom with 7 nonshared neighbors; the cluster is also connected to 4 In atoms with 4 nonshared neighbors resulting in multiple 3-, 4-, and 5-atom loops. Another realization has only two 3-atom loops and a long chain of nonshared undercoordinated In atoms, Fig. 14(b). This arrangement spreads out the lowest-ECN shortest In-In distance pairs into separate defect structures, causing the corresponding defect states to be closer to each other in energy, at −1.2, −1.6, and −1.9 eV, with an additional deep state at −2.9 eV. Similarly, the configuration

with no starlike crossing and the longest chain, Fig. 14(a), has one deep state at –3 eV and three localized states, –1.5, –1.9, and –2.3 eV. While photoillumination with visible or UV light may excite all of the defects, the shallower states may be sensitive to applied voltage or thermal stress, causing instabilities.

The widest coordination distribution among different realizations is found in a-In$_{54}$O$_{77}$, Fig. 4(a). Accordingly, this oxygen stoichiometry shows the widest distribution of the defect formation energies, Fig. 4(b), and in agreement with our discussion above, the a-In$_{54}$O$_{77}$ cases exhibit the widest energy spread of the defect states and the highest localization of the states in the vicinity of the Fermi level among all stoichiometries, Fig. 9(b). This finding highlights an important structure-property relationship in amorphous oxide semiconductors.

VIII. COMPARISON OF METALLIC FORMATIONS IN CRYSTALLINE AND AMORPHOUS OXIDES

As mentioned in the Introduction, highly nonstoichiometric crystalline In$_2$O$_{2.5}$ grown in an argon atmosphere shows metallic nanoclusters embedded in a bixbyite indium oxide matrix [19]. Similarly, nanocomposite In-Sn-O films exhibit phase separation between the stoichiometric crystalline oxide with insulating properties and the embedded metallic (In and Sn) nanoinclusions with percolation-like conductivity and a superconducting transition at 6 K [20–23].

In amorphous indium oxide, the formation of metallic bonds occurs already in nearly stoichiometric oxides, i.e., at oxygen stoichiometry of 2.926: in a-In$_{54}$O$_{79}$, the shortest In-In distance for a pair of nonshared In atoms is found to be 2.81 Å—significantly shorter than the shortest nonshared In-In distance (3.58 Å) in crystalline In$_2$O$_{2.94}$ with an oxygen vacancy defect [29] and also shorter than the In-In distance in elemental In metal (3.26 Å). As the oxygen stoichiometry decreases, the number of nonshared In neighbors for undercoordinated In atoms increases, Fig. 12, and in a-In$_{54}$O$_{76}$ (In$_2$O$_{2.815}$), percolation-like distribution of the nonshared In-In metallic formations becomes intricate and diverse, Fig. 14, with a strong tendency for single-atom chains, as discussed in the previous section. This ability of the amorphous indium oxide to spread out individual metallic bonds throughout the disordered structure instead of promoting their clustering that would enable growth of metallic nanoinclusions is the key feature that distinguishes the amorphous material's response to oxygen reduction from the behavior observed in crystalline oxides. Indeed, crystalline indium oxide exhibits phase separation between stoichiometric insulating In$_2$O$_3$ and the embedded metallic In nanoclusters detected by x-ray diffraction analyses [19]. In marked contrast, in amorphous indium oxide, the number of fully coordinated (ECN>5.5) In atoms is only 50% even in the perfectly stoichiometric a-In$_{54}$O$_{81}$, and it decreases to 34% for a-In$_{54}$O$_{76}$. The low numbers of fully coordinated In atoms prevent the nucleation of bixbyite In$_2$O$_3$ where all In atoms are octahedrally coordinated (ECN=5.6–6.0). Thus, the results of this work reveal that not only is the metallic In-In bond distribution relatively uniform within the highly nonstoichiometric oxide structure, but also that the In coordination in the entire oxide matrix is affected by oxygen deficiency leading to a more uniform coordination morphology as compared to crystalline nanocomposites.

We note here that the amorphous structures with higher oxygen stoichiometries, 3.000 and 2.963, exhibit only weak (unstable) In-In pairs with shortest nonshared distances of 3.65 and 3.53 Å, respectively, among 10 DFT-PBE optimized structures for each stoichiometry. The In-In distances belong to corner-shared distribution, Fig. 8(a), yet these pairs of In do not share any oxygen atoms with each other, hence we can classify them as undershared. The metallic bonding for these nonshared In-In pairs is weak (given the relatively long In-In distances) and do not cause substantial electron localization, Fig. 9(b). We should also mention that the shortest nonshared In-In distances during the MD run at 300 K are 3.15 and 3.23 Å for the above oxygen stoichiometries, respectively; however, such short-distant "bonds" appear only for very short periods of time of several fs, hence they are unstable.

The presence and distribution of metallic networks reported in this work highlight two important characteristics of amorphous indium oxide. First, due to the shallow metal-metal defects even in weakly substoichiometric In$_2$O$_{3-x}$, the observed carrier concentration in amorphous indium oxide is very high, $(3–5) \times 10^{20}$ cm^{-3} for the samples grown in oxygen partial pressure of 1–8 mTorr using the pulsed laser deposition (PLD) method [27,29,74]. Our calculated free-carrier concentrations, Table IV, are in excellent agreement with the measurements. Moreover, the number of carriers decreases only moderately, to 6×10^{19} cm^{-3}, when the oxygen partial pressure is increased to as much as 16 mTorr. This is in marked contrast to crystalline indium oxide, where the carrier concentration is two orders of magnitude lower, 5×10^{18} cm^{-3}, when grown by PLD at $p(O_2) = 8$ mTorr [27,29,74]. A high carrier density of 8×10^{20} cm^{-3} can be achieved in crystalline indium oxide only when samples are grown in an oxygen-free atmosphere and when oxygen stoichiometry is as low as 2.5 [19]. Second, we show that oxygen stoichiometry has a pronounced effect on the coordination morphology and distribution of metallic networks, as evident from the calculated electron velocity as a function of oxygen substoichiometry, Table IV. This explains the observed high sensitivity of the carrier mobility on an oxygen environment in amorphous indium oxide: the mobility changes from 9 to 50 cm^2/V s when the oxygen partial pressure increases from 1 to 8 mTorr [28]. For comparison, the electron mobility in stoichiometric In$_2$O$_3$ deposited in an oxygen-rich atmosphere is 5.5 cm^2/V s and it increases to 15.5 cm^2/V s in oxygen-deficient samples with oxygen stoichiometry of 2.5 [19]. The opposite mobility trends suggest that the scattering mechanisms are different in crystalline and amorphous oxides: in crystalline phases, the mobility is primarily limited by scattering on ionized impurities, whereas morphology and phonons are likely to govern the electron transport in amorphous oxides [28].

IX. HYDROGEN COMPENSATION IN HIGHLY NONSTOICHIOMETRIC AMORPHOUS OXIDE

In this work, we also study the changes in the structural and electronic properties of highly nonstoichiometric indium

oxides upon compensation with hydrogen. Hydrogen is common in amorphous metal oxides deposited by sputtering due to the presence of water vapor and also in samples that were grown by laser deposition techniques at low oxygen partial pressure and not encapsulated from the environment or brought in contact with H-containing layers in a device [75–78]. In amorphous In-Ga-Zn-O prepared by sputtering, hydrogen anion species and hydrogen in the form of a hydroxyl group were reported to each have concentrations of $>10^{20}$ cm^{-3} [79], while an order of magnitude higher concentration of hydrogen (about 5×10^{21} cm^{-3} or up to 7 at. %) was studied in amorphous indium oxide samples [77]. Substitutional H$^-$ was suggested to be responsible for negative bias illumination stress in amorphous metal oxides [80–82].

To determine the role of hydrogen in charge compensation and defect passivation, 10 H radicals were added to the amorphous In$_{54}$O$_{76}$ structure with the lowest total energy (among 10 realizations at the highest oxygen nonstoichiometry considered above). The initial locations of H atoms were determined as random positions with only two constrains: (i) the nearest-neighbor (In or O) distance to the initial H location is at least 1.7 Å (which is comparable to the typical In-H bond length [83] in amorphous In-Ga-O), while at the same time it was found to be shorter than 2.1 Å, in accord with earlier work [83]; and (ii) the initial H-H distances are long enough (4.1 Å on average) to correspond to a fairly uniform distribution of 10 H radicals within the supercell. The random yet uniform placement of H atoms ensures that each H has a freedom to relax toward or away from undercoordinated In atoms. The resulting structure, a-In$_{54}$O$_{76}$H$_{10}$, corresponds to H concentration of 5.8×10^{21} cm^{-3}. Prior to 0 K relaxation of the H-doped structure, *ab initio* molecular-dynamics simulations at 300 K were performed for the initial structure containing 10 H atoms for 5000 steps using integration steps of 0.5 fs. It has been shown that MD simulations help find stable H defects in energetically preferable locations and, at the same time, optimize the structural morphology of amorphous metal oxides by facilitating bond reconfiguration [83]. After the MD simulations, the H-doped configuration was relaxed using the DFT-PBE approximation followed by the HSE06 calculations to determine the electronic and optical properties of the H-doped oxide. The results are summarized in Figs. 15 and 16.

First, we find that out of 10 H atoms added to the In$_{54}$O$_{76}$ structure, 9 formed In-H-In defects and 1 formed an In-OH defect. The shortest In-H distance for the former defects ranged from 1.69 to 1.90 Å, representing a weak In-H bonding, and the O-H distance for the latter defect is 1.00 Å. The calculated charge transfer confirms that hydrogen in the In-H-In defects acts as an acceptor, accumulating an additional electron density from nearby In atoms, whereas OH$^-$ with a strong covalent bonding corresponds to H being a donor. The results are in agreement with previous investigations of H defects in amorphous In-Ga-O [83]. From the structural analysis we find that the presence of H affects the coordination of the majority of In atoms in the supercell, not only those in the vicinity of hydrogen, Fig. 15(a). Among the In atoms that have one or more H neighbors at distances shorter than 1.95 Å, several increase their coordination with oxygen, and for several the coordination does not change. At the same time, a few In
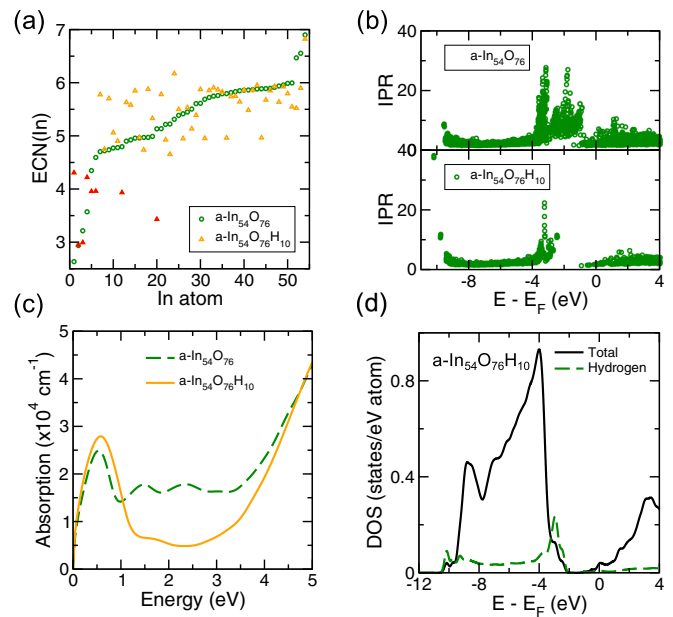

FIG. 15. (a) Effective coordination numbers for individual In atoms with oxygen neighbors in the lowest-energy realization for a-In$_{54}$O$_{76}$ (circle) and for the same In atoms after H doping and structural relaxation in a-In$_{54}$O$_{76}$H$_{10}$ (triangle). The In atoms that have one or more H neighbors at distances shorter than 1.95 Å are represented with filled red triangle symbols. Calculated (b) inverse participation ratio (IPR); (c) optical absorption; and (a) total and partial density of states (DOS) for amorphous In$_{54}$O$_{76}$ and a-In$_{54}$O$_{76}$H$_{10}$. The electronic properties are obtained using hybrid functional (HSE06) calculations for the structures optimized using DFT-PBE.

atoms reduced their coordination with oxygen upon H doping, Fig. 15(a). Strikingly, the coordination of many In atoms that do not have a hydrogen atom in their vicinity changed after H doping. This signifies that the entire amorphous structure undergoes a significant bond reconfiguration due to H doping. A notable fraction of In atoms increase their coordination from below 5 to well above 5.5, pointing out that the coordination morphology changes with H doping. The results highlight the fact that placing H at random initial positions throughout the structure and not directly at the localized defects, Fig. 16(a), not only models a realistic hydrogenation process, but also reveals the important role of structural reconfiguration in facilitating H passivation of strongly localized defects.

As expected, hydrogen is attracted to the oxygen-deficient regions with groups of undercoordinated undershared In atoms, cf., Fig. 14 and Sec. VII. The average In-O coordination of the In atoms that are the nearest neighbors of an H atom in relaxed a-In$_{54}$O$_{76}$H$_{10}$ was 3.54 prior to H doping. This is significantly lower than the average In-O coordination for the H-free structure, namely 5.30 (in the PBE optimized case). Accordingly, hydrogen effectively passivates the strongly localized states located within the band gap (located at −1 to −3 eV in H-free structure) and forms acceptorlike states near the top of the valence band, at −2.4 to −2.9 eV below the Fermi level, Fig. 15(b). The H passivation of the undercoordinated undershared In atoms significantly reduces the optical
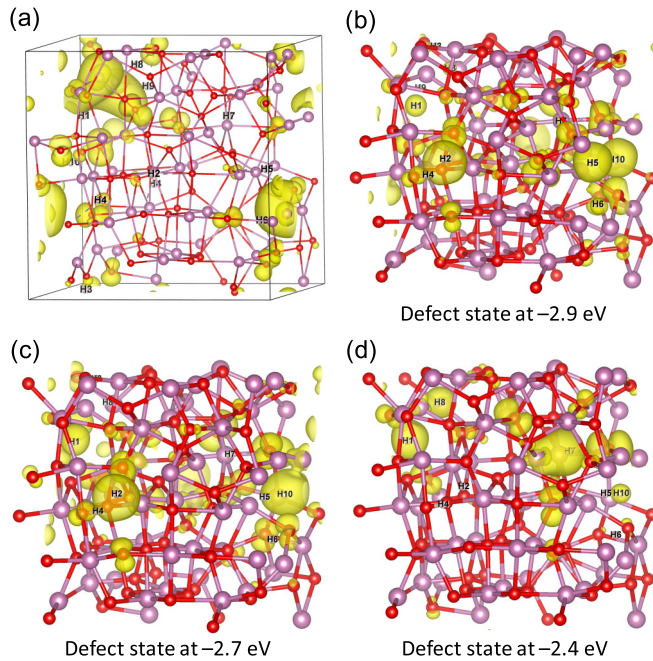
FIG. 16. (a) Initial locations of H with respect to the strongly localized defects in H-free structure of a-In$_{54}$O$_{76}$ showing that none of the 10 H radicals were placed directly at the defects represented by yellow charge-density contours. (b)–(d) Charge-density distribution calculated for the deep localized states formed near the top of the valence band in a-In$_{54}$O$_{76}$H$_{10}$.

absorption within the visible range as compared to the highly nonstoichiometric H-free case, Fig. 15(c). The calculated total and partial density of states, Fig. 15(d), reveals that the H states contribute primarily near the top of the valence band. Charge-density distributions calculated for the localized defect states above the top of the valence band confirm that the electron localization occurs on several H atoms as well as their undercoordinated In atoms and/or nonbonding O-p orbitals, Figs. 16(b)–16(d).

In addition to restoring optical transparency in the visible region, hydrogen doping is likely to significantly improve the stability of the material's response to thermal stress or applied voltage [84–86] because it narrows the range of activation energies of the defect states that trap the electrons and pushes the defect states from –1 eV or below in the H-free case to –2.4 eV or below after H doping, Fig. 15(b). In a separate work, it will be investigated whether the H-states located near the top of the valence band would be sufficiently sensitive to photoillumination with energies above 2.5 eV to play a role in photoswitching transients, as suggested earlier [87–92]. Importantly, hydrogen doping not only passivates the strongly localized gap states, but it also helps improve the electron mobility due to more uniform charge-density distribution in the conduction band associated with a widespread coordination rearrangement caused by H-doping, cf., Fig. 15(a). From the electronic structure calculations, we find that the states in the conduction band in a-In$_{54}$O$_{76}$H$_{10}$ have low IPR that reflects their delocalized nature. Comparing to the H-free case, the IPR values near the Fermi level are reduced by more than two times upon H doping, Fig. 15(b). Analysis of

the medium range structure reveals that H incorporation suppresses clustering of undercoordinated nonshared In-In pairs. The majority of the undercoordinated In atoms have only a single undercoordinated In with which it does not share an oxygen while being at a distance below 4.5 Å. Accordingly, H doping results in an increase of the average In-In distance for the undercoordinated (ECN<5.2) nonshared In-In pairs from 3.55 Å before H doping to 3.75 Å after H incorporation. The results signify that hydrogen further promotes the tendency for single-atom percolation-like chains of metallic In-In bonding, contributing to a better electron transport. Indeed, the electron velocity calculated along the [111] bandlike state at the energy where the band crosses the Fermi level increases from 7.6×10^4 m/s for the H-free configuration to 9.7×10^4 m/s after H doping.

We stress here that the formation of a single donor OH$^-$ defect in a-In$_{54}$O$_{76}$H$_{10}$ leads to the conductive state with the Fermi level located at 0.9 eV above the conduction-band bottom and a large concentration of free carriers as signified by the height of the Drude peak in the calculated absorption, Fig. 15(c). Indeed, the integrated density of states calculated within an energy range of −0.1 to 0.1 eV that represents free-carrier concentration is 6.0×10^{20} cm^{-3}, which is larger as compared to H-free a-In$_{54}$O$_{76}$, 5.6×10^{20} cm^{-3}, Table IV. Importantly, the results imply that unlike crystalline indium oxide where H serves as a dopant upon O substitution, hydrogen is not a donor in amorphous oxide; instead it affects carrier concentration indirectly by controlling the degree of electron localization and binding energy of oxygen defects associated with undercoordinated In-In.

Finally, we find that the presence of extended metallic networks in highly nonstoichiometric indium oxide leads to the formation of defect complexes such as In-H-H-In and In-OH-H-In with H-H distances of 2.4 Å and as short as 1.5 Å, respectively. These defects are likely to be less stable than the most common In-H-In and In-OH defects found in this work and reported earlier [79,83], and they may play an important role in H mobility and structural reconfiguration. Therefore, further investigations of the formation of H defect complexes and their stability at elevated temperatures are warranted.

X. CONCLUSIONS

In summary, the structural and electronic properties of amorphous In$_2$O$_{3-x}$ with $x = 0$–0.185 obtained via *ab initio* molecular dynamics simulations and accurate hybrid density-functional calculations are thoroughly investigated to establish the formation and microscopic features of oxygen defects in the disordered metal oxide. The results of this work reveal the key feature that distinguishes the amorphous material's response to oxygen reduction from the behavior observed in crystalline oxides, namely the tendency of the disordered ionic oxide to lower the coordination of a large fraction of In atoms and, at lower oxygen content, to spread the individual metallic In-In bonds associated with highly undercoordinated nonshared pairs or clusters of In atoms throughout the amorphous structure in a percolation-like single-atom chain.

Because of the collective response of the disordered metal oxide to the lack of oxygen, multiple descriptors for the local

(nearest-neighbor) In structure (such as the effective In-O coordination, In-O distance, or In-O polyhedral distortion) must be considered in combination with next-nearest-neighbor(s) distances, coordination, and sharing in order to accurately predict the degree of electron localization or the binding energy of the defects. Based on the derived structure-property relationships, we illustrate how the metallic network morphology gradually becomes more complex as the oxygen content decreases, and we identify the key features that lead to electron localization.

The results of this work provide a microscopic explanation of an increased number of free carriers combined with a good carrier mobility in the disordered indium oxide as compared to its crystalline counterpart. The extended nature of metallic percolation-like networks supports the coexistence of shallow and localized defects, whereas annealing in an oxygen environment or hydrogen compensation will promote a more uniform coordination morphology with no or deep defects (at 2–3 eV below the Fermi level) that cannot scatter free electrons. Our calculated carrier concentrations, electron velocities, and deep defect densities as a function of oxygen content are in excellent agreement with available experimental observations.

Given the striking differences between the structural and electronic properties of oxygen defects in crystalline and amorphous indium oxide, one should expect significant changes in carrier concentration and mobility during crystallization which occurs in In_2O_3 at low temperature [27]. Last but not least, understanding the structural features of metallic formations will help future studies of hydrogen passivation, the formation of H defect complexes, and H mobility throughout the disordered oxide as well as the relaxation dynamics in both H-free and H-doped indium oxide.

[1] K. Chopra, S. Major, and D. Pandya, Thin Solid Films **102**, 1 (1983).

[2] A. L. Dawar and J. C. Joshi, J. Mater. Sci. **19**, 1 (1984).

[3] H. Hartnagel, *Semiconducting Transparent Thin Films* (Institute of Physics, Bristol, UK, 1995).

[4] D. S. Ginley and C. Bright, MRS Bull. **25**, 15 (2000).

[5] J. F. Wager, D. A. Keszler, and R. E. Presley, *Transparent Electronics* (Springer, New York, 2008), Vol. 112.

[6] *Transparent Electronics: From Synthesis to Applications*, edited by A. Facchetti and T. Marks (Wiley, Chichester, UK, 2010).

[7] H. Hosono and D. C. Paine, *Handbook of Transparent Conductors* (Springer, New York, 2010).

[8] P. Barquinha, R. Martins, L. Pereira, and E. Fortunato, *Transparent Oxide Electronics: From Materials to Devices* (Wiley, Chichester, UK, 2012).

[9] K. Ellmer, Nat. Photon. **6**, 809 (2012).

[10] E. Fortunato, P. Barquinha, and R. Martins, Adv. Mater. **24**, 2945 (2012).

[11] C. Kilic and A. Zunger, Phys. Rev. Lett. **88**, 095501 (2002).

[12] C. G. V. de Walle, Phys. Status Solidi B **229**, 221 (2002).

[13] I. Tanaka, K. Tatsumi, M. Nakano, and H. Adachi, J. Am. Ceram. Soc **85**, 68 (2002).

[14] S. Lany and A. Zunger, Phys. Rev. Lett. **98**, 045501 (2007).

[15] P. Reunchan, X. Zhou, S. Limpijumnong, A. Janotti, and C. G. V. de Walle, Curr. Appl. Phys. **11**, S296 (2011).

[16] Q. Hou, J. Buckeridge, T. Lazauskas, D. Mora-Fonz, A. A. Sokol, S. M. Woodley, and C. R. A. Catlow, J. Mater. Chem. C **6**, 12386 (2018).

[17] J. E. Medvedeva and C. L. Hettiarachchi, Phys. Rev. B **81**, 125116 (2010).

[18] A. Murat, A. U. Adler, T. O. Mason, and J. E. Medvedeva, J. Am. Chem. Soc. **135**, 5685 (2013).

[19] M. Nistor, W. Seiler, C. Hebert, E. Matei, and J. Perrière, Appl. Surf. Sci. **307**, 455 (2014).

[20] M. Nistor, A. Petitmangin, C. Hebert, and W. Seiler, Appl. Surf. Sci. **257**, 5337 (2011).

[21] M. Nistor, J. Perrière, C. Hebert, and W. Seiler, J. Phys.: Condens. Matter **22**, 045006 (2010).

[22] J. Perrière, C. Hebert, A. Petitmangin, X. Portier, W. Seiler, and M. Nistor, J. Appl. Phys. **109**, 123704 (2011).

[23] E. Millon, M. Nistor, C. Hebert, Y. Davila, and J. Perrière, J. Mater. Chem. **22**, 12179 (2012).

[24] H. Hosono, M. Yasukawa, and H. Kawazoe, J. Non-Cryst. Solids **203**, 334 (1996).

[25] K. Nomura, H. Ohta, A. Takagi, T. Kamiya, M. Hirano, and H. Hosono, Nature (London) **432**, 488 (2004).

[26] H. Hosono, J. Non-Cryst. Solids **352**, 851 (2006).

[27] D. B. Buchholz, Q. Ma, D. Alducin, A. Ponce, M. Jose-Yacaman, R. Khanal, J. E. Medvedeva, and R. P. H. Chang, Chem. Mater. **26**, 5401 (2014).

[28] J. E. Medvedeva, D. B. Buchholz, and R. P. H. Chang, Adv. Electron. Mater. **3**, 1700082 (2017).

[29] J. E. Medvedeva, I. A. Zhuravlev, C. Burris, D. B. Buchholz, M. Grayson, and R. P. H. Chang, J. Appl. Phys. **127**, 175701 (2020).

[30] H.-X. Deng, S.-H. Wei, S.-S. Li, J. Li, and A. Walsh, Phys. Rev. B **87**, 125203 (2013).

[31] E. Fortunato, D. Ginley, H. Hosono, and D. C. Paine, MRS Bull. **32**, 242 (2007).

[32] T. Kamiya, K. Nomura, and H. Hosono, J. Display Technol. **5**, 273 (2009).

[33] J. C. Park, S. Kim, S. Kim, C. Kim, I. Song, Y. Park, U.-I. Jung, D. H. Kim, and J.-S. Lee, Adv. Mater. **22**, 5512 (2010).

[34] T. Kamiya, K. Nomura, and H. Hosono, Sci. Tech. Adv. Mater. **11**, 044305 (2010).

[35] J. S. Park, W.-J. Maeng, H.-S. Kim, and J.-S. Park, Thin Solid Films **520**, 1679 (2012).

[36] A. Nathan, S. Lee, S. Jeon, and J. Robertson, J. Display Technol. **10**, 917 (2014).

[37] W. Cao, J. Li, H. Chen, and J. Xue, J. Photon. Energy **4**, 040990 (2014).

[38] X. Yu, T. J. Marks, and A. Facchetti, Nat. Mater. **15**, 383 (2016).

[39] A. Aliano, A. Catellani, and G. Cicero, Appl. Phys. Lett. **99**, 211913 (2011).

[40] M. Kim, I. J. Kang, and C. H. Park, Curr. Appl. Phys. **12**, S25 (2012).

[41] C. J. Benmore, G. B. González, O. L. G. Alderman, S. K. Wilke, J. L. Yarger, K. Leinenweber, and J. K. R. Weber, J. Phys. Condens. Matter **33**, 194001 (2021).

[42] A. Walsh, J. L. F. Da Silva, and S.-H. Wei, Chem. Mater. **21**, 5119 (2009).

[43] W. Körner, P. Gumbsch, and C. Elsässer, Phys. Rev. B **86**, 165210 (2012).

[44] W. Körner and C. Elsässer, Thin Solid Films **555**, 81 (2014).

[45] S. Sallis, N. F. Quackenbush, D. S. Williams, M. Senger, J. C. Woicik, B. E. White, and L. F. J. Piper, Phys. Status Solidi A **212**, 1471 (2015).

[46] W. Körner, D. F. Urban, and C. Elsässer, Phys. Status Solidi A **212**, 1476 (2015).

[47] M. J. Wahila, K. T. Butler, Z. W. Lebens-Higgins, C. H. Hendon, A. S. Nandur, R. E. Treharne, N. F. Quackenbush, S. Sallis, K. Mason, H. Paik, D. G. Schlom, J. C. Woicik, J. Guo, D. A. Arena, B. E. White, G. W. Watson, A. Walsh, and L. F. J. Piper, Chem. Mater. **28**, 4706 (2016).

[48] E. Rucavado, Q. Jeangros, D. F. Urban, J. Holovský, Z. Remes, M. Duchamp, F. Landucci, R. E. Dunin-Borkowski, W. Körner, C. Elsässer, A. Hessler-Wyser, M. Morales-Masis, and C. Ballif, Phys. Rev. B **95**, 245204 (2017).

[49] M. J. Wahila, Z. W. Lebens-Higgins, K. T. Butler, D. Fritsch, R. E. Treharne, R. G. Palgrave, J. C. Woicik, B. J. Morgan, A. Walsh, and L. F. J. Piper, APL Mater. **7**, 022509 (2019).

[50] S. Husein, J. E. Medvedeva, J. D. Perkins, and M. I. Bertoni, Chem. Mater. **32**, 6444 (2020).

[51] A. Murat and J. E. Medvedeva, Phys. Rev. B **85**, 155101 (2012).

[52] G. Kresse and J. Hafner, Phys. Rev. B **47**, 558 (1993).

[53] G. Kresse and J. Hafner, Phys. Rev. B **49**, 14251 (1994).

[54] G. Kresse and J. Furthmuller, Phys. Rev. B **54**, 11169 (1996).

[55] G. Kresse and J. Furthmuller, Comput. Mater. Sci. **6**, 15 (1996).

[56] P. Hohenberg and W. Kohn, Phys. Rev. **136**, B864 (1964).

[57] W. Kohn and L. J. Sham, Phys. Rev. **140**, A1133 (1965).

[58] J. P. Perdew, K. Burke, and M. Ernzerhof, Phys. Rev. Lett. **77**, 3865 (1996).

[59] J. P. Perdew, K. Burke, and M. Ernzerhof, Phys. Rev. Lett. **78**, 1396(E) (1997).

[60] P. E. Blochl, Phys. Rev. B **50**, 17953 (1994).

[61] G. Kresse and D. Joubert, Phys. Rev. B **59**, 1758 (1999).

[62] J. E. Medvedeva, *Amorphous Oxide Semiconductors: IGZO and Related Materials for Display and Memory*, edited by H. Hosono (Wiley, Chichester, UK, 2022).

[63] R. Hoppe, Angew. Chem., Int. Ed. Engl. **9**, 25 (1970).

[64] R. Hoppe, S. Voigt, H. Glaum, J. Kissel, H. P. Muller, and K. Bernet, J. Less-Common Met. **156**, 105 (1989).

[65] J. Heyd, G. E. Scuseria, and M. Ernzerhof, J. Chem. Phys. **118**, 8207 (2003).

[66] J. Heyd, J. E. Peralta, G. E. Scuseria, and R. L. Martin, J. Chem. Phys. **123**, 174101 (2005).

[67] W. Tang, E. Sanville, and G. Henkelman, J. Phys.: Condens. Matter **21**, 084204 (2009).

[68] J. Strand, M. Kaviani, D. Gao, A.-M. El-Sayed, V. V. Afanas'ev, and A. L. Shluger, J. Phys.: Condens. Matter **30**, 233001 (2018).

[69] K. Momma and F. Izumi, J. Appl. Crystallogr. **44**, 1272 (2011).

[70] J. E. Medvedeva, *Transparent Electronics: From Synthesis to Applications*, edited by A. Facchetti and T. Marks (Wiley, Chichester, UK, 2010), pp. 1–29.

[71] R. Khanal, D. B. Buchholz, R. P. H. Chang, and J. E. Medvedeva, Phys. Rev. B **91**, 205203 (2015).

[72] S. L. Moffitt, Q. Zhu, Q. Ma, A. F. Falduto, D. B. Buchholz, R. P. H. Chang, T. O. Mason, J. E. Medvedeva, T. J. Marks, and M. J. Bedzyk, Adv. Electron. Mater. **3**, 1700189 (2017).

[73] F. Gunkel, D. V. Christensen, Y. Z. Chen, and N. Pryds, Appl. Phys. Lett. **116**, 120505 (2020).

[74] D. B. Buchholz, L. Zeng, M. J. Bedzyk, and R. P. Chang, Prog. Nat. Sci.: Mater. Int. **23**, 475 (2013).

[75] T. Koida, H. Fujiwara, and M. Kondo, Jpn. J. Appl. Phys. **46**, L685 (2007).

[76] H. F. Wardenga, M. V. Frischbier, M. Morales-Masis, and A. Klein, Materials **8**, 561 (2015).

[77] S. Husein, M. Stuckelberger, B. West, L. Ding, F. Dauzou, M. Morales-Masis, M. Duchamp, Z. Holman, and M. I. Bertoni, J. Appl. Phys. **123**, 245102 (2018).

[78] R. Muydinov, A. Steigert, M. Wollgarten, P. P. Michałowski, U. Bloeck, A. Pflug, D. Erfurt, R. Klenk, S. Körner, I. Lauermann *et al.*, Materials **12**, 266 (2019).

[79] K. Nomura, T. Kamiya, and H. Hosono, ECS J. Solid State Sci. Technol. **2**, P5 (2012).

[80] K. Hayashi, P. V. Sushko, Y. Hashimoto, A. L. Shluger, and H. Hosono, Nat. Commun. **5**, 3515 (2014).

[81] H. Tang, Y. Kishida, K. Ide, Y. Toda, H. Hiramatsu, S. Matsuishi, S. Ueda, N. Ohashi, H. Kumomi, H. Hosono *et al.*, ECS J. Solid State Sci. Technol. **6**, P365 (2017).

[82] H. Li, Y. Guo, and J. Robertson, Sci. Rep. **7**, 16858 (2017).

[83] J. E. Medvedeva and B. Bhattarai, J. Mater. Chem. C **8**, 15436 (2020).

[84] K. Hoshino, D. Hong, H. Q. Chiang, and J. F. Wager, IEEE Trans. Electron. Dev. **56**, 1365 (2009).

[85] P. Migliorato, M. Delwar Hossain Chowdhury, J. Gwang Um, M. Seok, and J. Jang, Appl. Phys. Lett. **101**, 123502 (2012).

[86] C.-H. Han, S.-S. Kim, K.-R. Kim, D.-H. Baek, S.-S. Kim, and B.-D. Choi, Jpn. J. Appl. Phys. **53**, 08NG04 (2014).

[87] T.-C. Fung, C.-S. Chuang, K. Nomura, H.-P. D. Shieh, H. Hosono, and J. Kanicki, J. Inf. Disp. **9**, 21 (2008).

[88] J. Luo, A. Adler, T. Mason, D. Bruce Buchholz, R. Chang, and M. Grayson, J. Appl. Phys. **113** (2013),.

[89] J. K. Jeong, J. Mater. Res. **28**, 2071 (2013).

[90] A. J. Flewitt and M. J. Powell, J. Appl. Phys. **115**, 134501 (2014).

[91] J. Luo and M. Grayson, MRS Adv. **1**, 3441 (2016).

[92] J. Luo, Ph.D. thesis, Northwestern University, 2016.